Crystal Structure of $Li_xNi_{2-x}O_2$ and a Lattice-Gas Model for the Order-Disorder Transition

by

Wu Li

B. Sc., Zhongshan University, 1985
M. Sc., Zhongshan University, 1988

A THESIS SUBMITTED IN PARTIAL FULFILLMENT
OF THE REQUIREMENTS FOR THE DEGREE OF
MASTER OF SCIENCE

in the Department
of
Physics

March 1992

ISBN 0-315-83693-8

APPROVAL

Name: Wu Li

Degree: Master of Science

Title of thesis: Crystal Structure of $Li_xNi_{2-x}O_2$ and a Lattice-Gas Model for the Order-Disorder Transition

Examining Committee:

Chairman: Prof. E. D. Crozier

Associate Prof. J. R. Dahn
Senior Supervisor

Assistant Prof. J. Bechhoefer

Prof. R. F. Frindt

Prof. M. Plischke
Examiner

Date Approved: March 27, 1992

PARTIAL COPYRIGHT LICENSE

I hereby grant to Simon Fraser University the right to lend my thesis, project or extended essay (the title of which is shown below) to users of the Simon Fraser University Library, and to make partial or single copies only for such users or in response to a request from the library of any other university, or other educational institution, on its own behalf or for one of its users. I further agree that permission for multiple copying of this work for scholarly purposes may be granted by me or the Dean of Graduate Studies. It is understood that copying or publication of this work for financial gain shall not be allowed without my written permission.

Title of Thesis/Project/Extended Essay

Crystal Structure of $LiMg_2Cl_3(OH)\cdot H_2O$ and a Lattice - Gas Model for the Order - Disorder Transition

Author: _____
(signature)

WU LI
(name)

April 5, 1992
(date)

Abstract

The crystal structure of $Li_xNi_{2-x}O_2$ for $0 \leq x \leq 1$ is determined. For $x<0.62$, $Li_xNi_{2-x}O_2$ has the disordered rocksalt structure. For $0.62 \leq x \leq 1.0$, Li and Ni atoms segregate into Li rich and Ni rich layers normal to one of the 4 (111) directions in the cubic lattice. This breaks the cubic symmetry and an apparently continuous transition to a hexagonal phase occurs. At $x=1$, alternate cation layers are nearly pure Li and pure Ni. The degree of order is quantified by defining an order parameter, η , which we take to be the difference in the Li composition of neighboring metal atom layers. Using X-ray diffraction and Rietveld profile refinement, we have measured η versus x. We model $Li_xNi_{2-x}O_2$ as a lattice of oxygen atoms into which cations (either Li or Ni) can be inserted, subject to the constraint that the number of cations equals the number of oxygen atoms. Interactions between cations on nearest and on next-nearest-neighbor sites are included, and the lattice gas model is solved using mean-field and Monte Carlo methods. We find that the nearest-neighbor interaction is not sensitive to the observed ordering and that we can describe the experimental variation of η versus x for an appropriate choice of the next-nearest-neighbor interaction.

Acknowledgements

I wish to thank Dr. Jeff Dahn for suggesting the research topic, and for his encouragement and advice throughout the entire research work. I would like to thank Dr. J. R. Reimers for his very useful assistance during this work. I am grateful to my fellow graduate students Hang Shi and Brian M. Way. I appreciate the assistance and work done by the physics secretarial and technical staff and by those in the Machine Shop. I also thank Dr. John Bechhoefer and Dr. Robert Frindt for serving on the committee.

Contents

List of Figures

List of Tables

1. Introduction

1.1 Rechargeable Batteries

Electrochemical energy storage will become more important as the shortage of fossil fuels and pollution grows more serious. Renewable energies such as solar or wind will be widely used energy sources if a more efficient method is found to store their energy. Electrical energy is the most convenient one to use, and rechargeable batteries can directly change chemical energy into electrical energy. However, energy densities of commercial secondary batteries (typically 100 $Whkg^{-1}$) are far below energy densities of non-renewable and polluting fuels such as gas or oil (12,000$Whkg^{-1}$). If the large difference between [1] theoretical (up to >1000 $Whkg^{-1}$) and practical energy densities of batteries were reduced considerably, then secondary batteries could be widely used in electric cars and other applications.

The periodic table is the best place to start looking for a suitable material for batteries. Electronegativity and atomic weight are initial factors to be considered for high electrochemical energy densities. The elements in the upper left corner should be candidates for the anode and the those in the upper right corner (except for the noble gases) for the cathodes without considering cost or safety factors. Although hydrogen is the lightest atom, it is not the best element for the anode since solid hydrogen does not exist at room temperature. Metal hydrides (e.g. H_xM) are used for the anodes in Ni-Metal hydrides cells which are rapidly replacing Ni-Cad cells in the marketplace. Lithium is the next material to be considered and it provides

the highest theoretical charge density (3860 $Ahkg^{-1}$). Other possible anode materials are Al (2980), Ca(1340), Na (1170), and Zn(820).

Secondary lithium batteries have some advantages over conventional technologies [2]. They can operate at room temperature and offer high energy density (up to 100 Whr/kg for AA-size cells). They can store energy for a long time (up to 5 to years) without much loss and offer high cell voltage (up to 3.5 volts per cell). However, safety problems have to be solved before they are widely available. Furthermore their cost is higher than conventional technologies.

Rechargeable Li batteries mainly consist of three materials, the negative electrode, the positive electrode and the electrolyte. Most electrolyte solvents are chosen from propylene or ethylene carbonate, 2-MeTHF, and DME [6]. The electrolyte salts are usually $LiAsF_6$, $LiCF_3SO_3$, $LiPF_6$, or $LiN(CF_3SO_2)_2$. High rate lithium batteries have very thin electrodes (100 microns thick) because these liquid electrolytes usually have conductivities about two orders of magnitude lower than the aqueous electrolytes used in Nickel-Cadmium cells. Thin electrodes are used to lower the dissipation inside the batteries. Polymer electrolytes like $LiN(CF_3SO_2)_2$ /polyethylene oxide (PEO) can not achieve good rate capabilities without extremely thin electrodes since conductivities of the electrolytes are two orders of magnitude lower than those of liquid non-aqueous electrolytes.

Before the serious safety problem associated with secondary cells was recognized, metallic Li anodes or Li-Al alloys were used as anodes throughout most of the 1980's. Other alloy systems such Li-Woods metal appeared in some commercial cells. After the very poor safety record was reported [7], new

technologies were not used in battery fabrication without careful consideration of safety. Recently, attractive cells have been found where a second intercalation compound is chosen for the negative electrode [3, 4, 5]. The negative and positive electrodes are both intercalation materials and the Li atoms shuttle back and forth between the electrodes when a cell operates. Such cells have been called "rocking-chair" cells. Now, low surface area (<10 m^2/g) carbon is used for the negative electrode in these rocking chair cells

There are many materials used for the cathodes of rechargeable Li batteries. Many new technologies developed rapidly in 1980's because of many choices for the cathode and anode and for the electrolyte. On the other hand, much work must be done before a new technology can displace old ones. Many factors such as safety, good performance and cycle life are important for practical uses. It is very difficult to find a cathode material which satisfies all the needs for practical uses; here we just introduce some of the materials used for the cathodes. Many metal oxides have been studied carefully for their electrochemical properties; these include vanadium oxides, chromium oxides, manganese oxides, cobalt oxides and nickel oxides.

Vanadium oxides have been studied extensively as cathode materials. It has been found that Li atoms can intercalate into these materials. Some structural aspects regarding these compounds have been reviewed by Abraham [8]. Many reports appeared characterizing V_2O_5, LiV_3O_8, V_6O_{13} [9, 10, 12, 14]. X-ray diffraction, electrochemical and infrared techniques are common methods to investigate these materials.

Several steps in the voltage-composition profile occur during discharge of Li cells with crystalline V_2O_5 cathodes. Above 2.0 V, three charge equivalents

corresponding to $Li_3V_2O_5$ can be provided, which corresponds to a charge density of 440 $Ahkg^{-1}$. Theoretical energy densities up to 650 $Whkg^{-1}$ are achieved during slow discharge for primary Li/V_2O_5 cells [9]. However, good cycling behavior is observed only if x in $Li_xV_2O_5$ is limited to 1-1.5 [10]. It has been confirmed [29] that V_2O_5 is very sensitive to overdischarge and that V-O bo ds are broken for $x>1$.

$Li_{1+x}V_3O_8$ was introduced as a cathode material for Li cells by Nassau et al. in 1981 [11]. Every LiV_3O_8 unit can accept up to three more lithium atoms by chemical intercalation with butyllithium [12]. Li/LiV_3O_8 cells have a theoretical charge density of 280 $Ahkg^{-1}$ and a specific energy of 680 $Whkg^{-1}$. Its application is limited by the disadvantages of low electronic conductivity and high oxidizing capability which may result in electrolyte decomposition [13].

V_6O_{13} was used as a cathode material by Murphy et al. [14]. Much subsequent work concentrated on the electrochemical characteristics of V_6O_{13} and its performance in secondary Li cells with organic electrolytes. Each V_6O_{13} unit can accommodate up to 8 Li with butyllithium when nonstoichiometric. The highest capacity is obtained for $2.17<x<2.19$ in VO_x [15]. V_6O_{13} (n=8) has a large theoretical charge density (420 $Ahkg^{-1}$), but only six Li can be inserted reversibly in V_6O_{13} [16]. The discharge is divided into three main steps corresponding to the consecutive transfer of one, three, and four electrons. V_6O_{13} is practically insoluble in organic solvents in comparison to V_2O_5. This gives a low self-discharge rate and good shelf life.

Chromium oxides, CrO_x have been studied as cathode materials in the range $2\leq x\leq 2.67$ [17]. Yamamoto et al. reported [20] that amorphous Cr_3O_8 is better

than crystalline Cr_3O_8 samples. Varta studied primary Li/CrO_x cells and obtained practical energy densities of 270 $Whkg^{-1}$ [18]. Toyoguchi et al. [19] developed coin-type Li/Cr_2O_5 secondary batteries which claimed practical energy densities of 170 $Whkg^{-1}$ and could give 400 cycles. Chromium oxides appear to offer very high theoretical energy densities when used as solid cathodes in Li cells.

MnO_2 is the most popular cathode materials for galvanic cells since it is cheap and has reasonable capacity and electrode potential. Currently, eight billion primary zinc/manganese dioxide batteries are produced each year [21]. MnO_2 has been investigated as a cathode material in primary Li cells since the 1970's [22]. Sony used to produce secondary Li batteries based on MnO_2 [23]. These AA cells offered very high practical energy densities of 125 $Whkg^{-1}$ and 240 Wh/l at discharge rates of C/2.5h (discharge the entire capacity in 2.5 hours) with an average voltage of 2.8V. It is claimed that these cells can achieve 1000 recharge cycles. Self-discharge is low at about 1% per month [23]. However, there are still some serious safety problems to solve before these cells can be really successful products. Moli Energy's Li/MnO_2 cells were similar in performance to the Sony cells.

Nickel oxides are another successful cathode material in commercial secondary cells. Ni/Cd cells are now used world-wide and their sales have reached US $ 1.3 billion per year. Nickel oxide has been considered as a cathode material in alkaline cells since 1887 [24]. Even though some patents appeared in 1900/1901, their electrochemistry is not yet fully understood .

The open circuit voltage of Li/Li_xCoO_2 cells is as high as 4.7V for x=0.07 [25]. Theoretical energy densities of 1070 $Whkg^{-1}$ can be obtained based on x=1 and

an average discharge voltage of 3.9V. But the high discharge voltage and oxidizing power of the Li_xCoO_2 can cause the decomposition the electrolyte, forming polymeric films on the electrode surface [26] and corroding the underlying metal support. Nevertheless, at least one company (Sony) is now exploiting the highly promising characteristics of $LiCoO_2$ for practical rechargeable batteries.

Many companies are working hard on rechargeable Li batteries. Early in the 1980's, Moli Energy Ltd. in Burnaby, B. C., developed the first commercial AA-size rechargeable Li battery with 300 cycles. The cell had thin electrodes, using Li-125μm and MoS_2 on Al foil as electrodes. These Li/MoS_2 AA-size cells stored about 1.4 Wh of energy and weighed 21 grams. However, several safety incidents involving the cells [27] forced their withdrawal from the market. Li/MnO_2 AA-size cells were announced in the late 1980's by several companies (Sony Energytec, Moli Energy Ltd. and Matsushita). Those constructed at Moli Energy stored about 2 Wh of energy, weighed about 19 grams and had a 200 cycle life time. Because of safety problems, these cells were never introduced in the marketplace. On the other hand, the safety problems in Li-alloy/MnO_2 coin cells are rare since the cells are very small.

Now it is understood that the poor safety of rechargeable Li electrodes is caused by the large area of contact between the cycled Li and the electrolyte. This unstable surface becomes larger and larger when the cells are cycled and thermal and/or electrical abuse results in the unacceptable situations. Apparently, if the surface area of the negative could be kept small or if less active materials were used, the poor safety could be improved.

In the rocking chair approach, both negative and positive electrodes are intercalation compounds with high reversibilities. The surface area of the powders used as electrodes is kept small during cycling to ensure the conditions for safety. Sony has fabricated $LiCoO_2$/Carbon rechargeable batteries in a variety of sizes. The AA size cells can store about 1.4 Wh energy and be cycled up to 1200 times. Many other companies are now concentrating on the rocking chair approach to construct rechargeable Li batteries.

$LiNiO_2$ is another choice for the cathode. Many studies have been made to understand the electrochemical characteristics of Li-Ni-O materials. Since this thesis concentrates on $Li_xNi_{2-x}O_2$, it is very useful elaborate more about work done on that material.

1.2 Li-Ni-O Materials

NiO has the rock-salt structure. Li-Ni-O compounds usually have one oxygen atom per metal atom and are normally based on layers of close-packed oxygen atoms . $LiNiO_2$ was first prepared by Dyer et al [30]. Goodenough et al. [31, 32] and Bronger et al. [33] studied the phases in the solid-solution series $Li_xNi_{2-x}O_2$ ($0<x<1$). They showed that a disordered rock-salt structure exists for $x<0.56$ and that partial cation ordering occurs for $x>0.6$. They suggested that there is an ordering of the cations in the alternate $(111)_C$ ((111) in the cubic structure) planes and calculated the order parameter as a function of x based on the magnetic measurements and the analysis of X-ray diffraction patterns.

$LiNiO_2$ has the space group $R\ \bar{3}\ m$ with a_h=2.876Å and c_h=14.19Å. Other Li-Ni-O compounds exist besides $LiNiO_2$. Additional lithium can also be inserted electrochemically into $LiNiO_2$ to form a new Li_2NiO_2 phase (1T-Li_2NiO_2) with the $Ni(OH)_2$ structure [28]. When the additional Li is removed from Li_2NiO_2, the host lattice reverts to the $LiNiO_2$ structure, but there is substantial hysteresis in the voltage of $Li/Li_{1\pm y}NiO_2$ cells during this phase transition. The analogous phase, Li_2CoO_2, does not form when additional Li is added to $LiCoO_2$ by electrochemical methods. The transformation between these phases can be made by displacing O-Ni-O sheets normal to the c-axis. In the 3R-$LiNiO_2$ structure, all cations are octahedrally coordinated by oxygen and the Ni layers adopt ABCABC-stacking to maximize the distance between cations. When Li_2NiO_2 forms, additional lithium must be accommodated within the lithium containing layers. This necessitates a filling of the tetrahedral sites accompanied by a displacement of the O-Ni-O sheet so that the Ni layers exhibit AAA-stacking; this maximizes the distance between cations. This phase has the space group $P\ \bar{3}\ m1$.

The orthorhombic phase of Li_2NiO_2 was reported by Rieck and Hoppe [34]. who found a=3.843Å, c=2.779Å. The 1T-Li_2NiO_2 phase is changed to the orthorhombic phase when heated to 500°C.

Room-temperature electrochemical extraction of lithium from nearly stoichiometric, layered $LiNiO_2$ gives the solid solution system $Li_{1-x}NiO_2$. The normal spinel $Li[Ni_2]O_4$ is formed by a 200°C anneal of the metastable layered compound $Li_{0.5}NiO_2$ obtained by electrochemical extraction lithium from $LiNiO_2$ at room temperature [35].

In addition to structural studies, lithium nickel oxides have been studied as catalysts for the direct conversion of methane to higher hydrocarbons through oxidative coupling [36] and for other oxidation reactions such as C-O oxidation [37]. The selectivities observed for oxidative coupling of methane are comparable to those of other catalysts such as Li/MgO [38]. The good electronic conductivity also allows the use of lithium nickel oxides as an electrocatalyst for methane oxidation and improved selectivities have been reported under conditions where oxygen ions were electrochemically pumped away from the oxide catalytic surface. Electrocatalytic and oxygen exchange kinetic data indicate that oxide ion diffusion is significant, but little quantitative information is currently available

The "rocking-chair" rechargeable batteries that use lithium intercalation compounds for the positive and negative electrodes are safer than batteries that contain free-lithium metal because of the unstable character of lithium metal. $LiNiO_2$ [4, 28] has been proposed as an electrode material in secondary Li batteries, because Li can be electrochemically de-intercalated from this material to form $Li_{1-y}NiO_2$. Li_xC_6 is used as the anode which has a chemical potential close to that of Li metal. Cells with $LiNiO_2$ as the cathode with petroleum coke as the anode have been made, and they have high energy density, long cycle life, excellent high-temperature performance, and low self-discharge rates. Furthermore they can be repeatedly discharged to zero volts without damage, and are easily fabricated.

The performance of the cells depends on the stoichiometry of $Li_xNi_{2-x}O_2$ used in the cell. Ni atoms enter the Li layers and presumably these Ni atoms impede the diffusion of Li. Therefore, it is important to know how much Ni

enters the Li layers as a function of x, so it is necessary to have a careful structural study on this solid solution.

1.3 Studies of Order-Disorder

X-ray diffraction is one well developed method to study order-disorder transitions. Binary alloys, such as β–CuZn, are typical examples where order-disorder transitions have been investigated by the X-ray diffraction methods. Review articles include those by Nix and Shockley [39], Lipson [40], Guttman [41] and Gerold [42]. $Li_xNi_{2-x}O_2$ is not a binary alloy (it is a pseudobinary), but its order-disorder structure can be studied in a way similar to that which has been successful on the binary alloy of β–Brass.

The β brass phase of the copper zinc system occurs in a small range of composition near the equiatomic composition CuZn. The atoms are found in the ordered structure if brought to equilibrium at low temperature. In the ordered structure, the cube corners are occupied by the copper atoms while the cube center positions are occupied by the zinc atoms as in the CsCl structure type. This is a body-centered-cubic structure. At somewhat higher temperatures, the structure is not perfectly ordered, but most of the copper are still on the cube corners and the zinc atoms are still on the cube center positions. The long-range order still exists, but it is only partial long-range order. The critical temperature is around T_c=460°C depending on the exact composition. The long-range order disappears above this temperature, and

the corner and center positions are occupied randomly by copper and zinc atoms. Although long-range order vanishes above the critical temperature, short-range order still exists. This means that the probability of occupation of certain positions are affected by the occupation of close-neighbor positions but not by the more distant positions.

For long-range order in binary compositions, there are two kinds of atoms A and B and two kinds of positions, α–sites and β–sites. Perfect long-range order is defined as that which occurs when the α–sites are all occupied by A-atoms and the β-sites by B-atoms. If N is the number of atoms in the sample, $N_A=x_AN$ and $N_B=x_B\,N$, such that $x_A+x_B=1$, where x_A and x_B are the atom fractions. If y_α and y_β are the fractions of α-sites and β-sites, then $y_\alpha+y_\beta=1$. The number of each kind of site is given by $N_\alpha=y_\alpha N$ and $N_\beta=y_\beta N$.

Nix and Shockley introduced four important parameters: r_α for fraction α-sites occupied by the right atom; w_α for fraction of α-sites occupied by the wrong atom; r_β for fraction of β-sites occupied by the right atom; w_β for fraction of β-sites occupied by the wrong atom. Suppose each site is occupied by one atom and there are no vacancies. Two relations between the parameters are immediately obvious:

$$r_\alpha+w_\alpha=1 \qquad \text{and } r_\beta+w_\beta=1,$$

since the fraction of the sites occupied by A-atoms equals the fraction of A-atoms and the fraction of the sites occupied by B-atoms equals the fraction of B-atoms. There are two equations, which are easily obtained

$$y_\alpha r_\alpha+y_\beta w_\beta=x_A \qquad \text{and } y_\beta r_\beta+y_\alpha w_\alpha=x_B$$

It is convenient to define the Bragg-Williams long-range order parameter η for nonstoichiometric compositions that η is linearly proportional to $(r_\alpha+r_\beta)$ with $\eta=0$ for a completely random arrangement and $\eta=1$ for the completely ordered stoichiometric phase with $r_\alpha=r_\beta=1$. Then the long-range order parameter is expressed in the simple form:

$$\eta=r_\alpha+r_\beta-1$$

The parameter η can not reach its maximum value of unity except for a stoichiometric composition with perfect order-range order. With such a definition of order parameter, the structure factors for nonstoichiometric compositions are proportional to η for the Miller index related to this ordered structure. The order parameter η is thus easy to observe in X-ray experiments.

2. Sample Preparation

Li_2CO_3 and NiO are usually used as the starting materials to prepare $Li_xNi_{2-x}O_2$. When Li_2CO_3 and NiO in the proper ratio are ground and heated between 650°C and 850°C, the Li_2O resulting from the decomposition of Li_2CO_3 combines with NiO to form $Li_xNi_{2-x}O_2$. This method is good for small x. However, since pure Li_2CO_3 only decomposes at high temperature (800°C) , we need more processing to form pure $Li_xNi_{2-x}O_2$ with x near 1 because of the remaining Li_2CO_3 phase. At higher temperature there is a loss of Li due to volatilization of Li salts.

Here $Li_xNi_{2-x}O_2$ samples were prepared by reacting stoichiometric mixtures of $LiOH \bullet H_2O$ and $Ni(OH)_2$. The powders were ground with a mortar and pestle and then heated at 700°C for 2 hours in air followed by slow cooling over several hours to room temperature. LiOH reacts rapidly with NiO, (which forms when $Ni(OH)_2$ decomposes around 300°C), which minimizes the Li loss due to extended heating that commonly occurs when Li_2CO_3 is used a starting material. Li_2CO_3 appeared when the Li:Ni ratio was more than 1. This could be avoided by carrying the reaction out under O_2 (Li_2O forms instead), but still we could not prepare single phase materials with $x>1$.

3. X-ray Diffraction

There are three factors which are considered in calculating the intensity of X-ray diffraction: scattering from electrons , scattering from an atom and scattering from crystal structures.

The results of scattering from electrons are derived from electromagnetic theory. An accelerated charge radiates, and the electric field produced by the accelerated charge is given by

$$\varepsilon = \frac{qa\sin\alpha}{c^2 R} \qquad (1.1)$$

where c is the velocity of light, a is the acceleration of the charge q, R is the distance between the charge and the observation point. α the angle between **R** and **a**. Figure 1a shows the directions of **a** , **R** and angle α. The observation point is P.

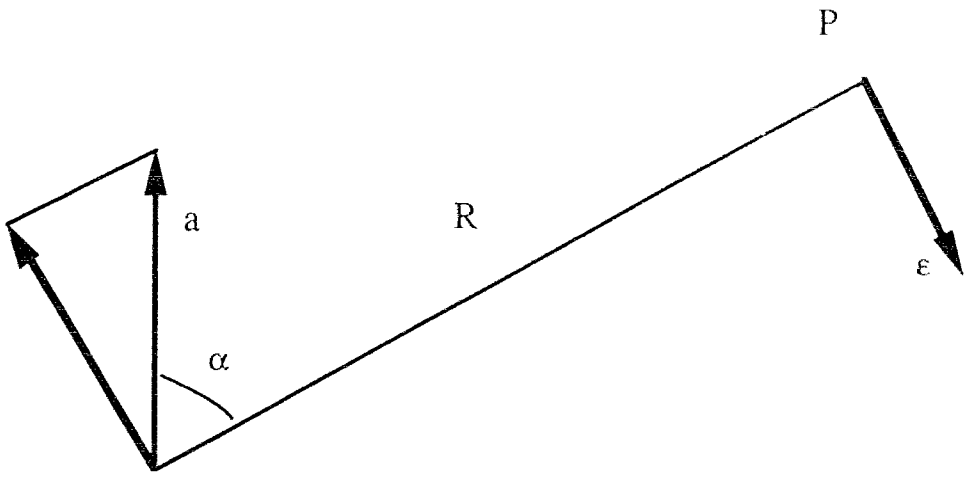

Figure 1a In classical electromagnetic theory, a charge q with acceleration a produces the electric field ε

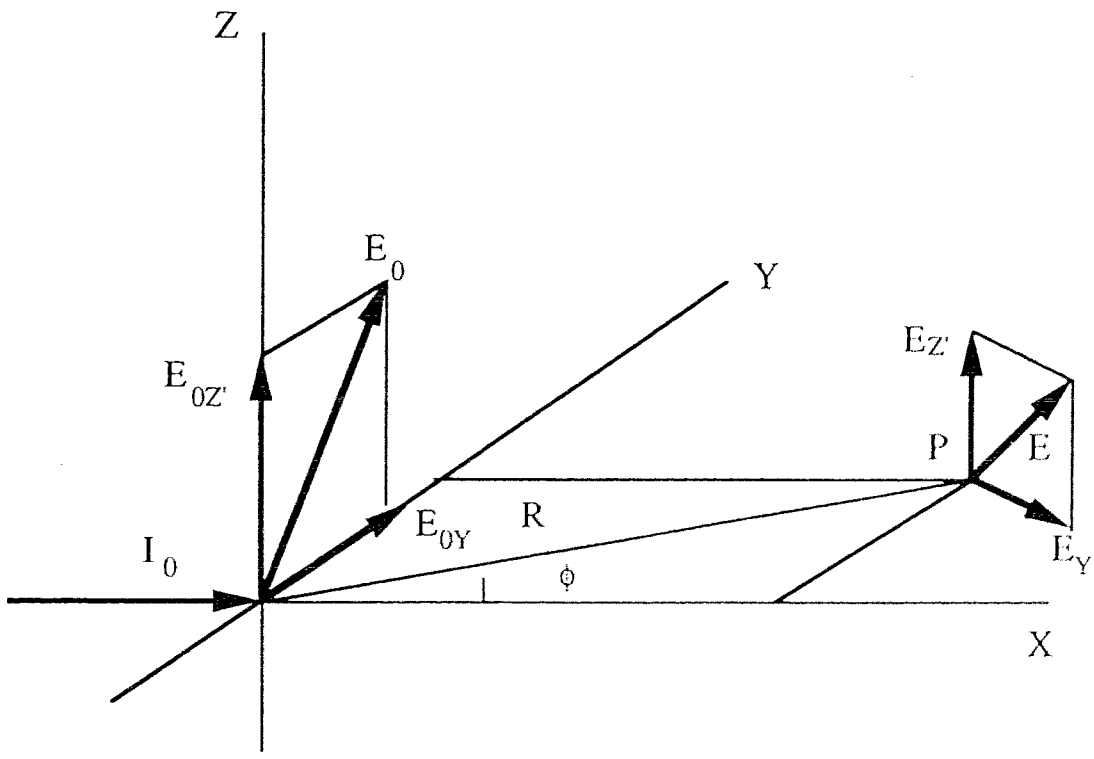

Figure 1b An unpolarized primary beam along X-axis is scattered by a single free electron at the origin

We consider a single free electron at the origin of figure 1b with an unpolarized primary beam directed along the X-axis. We choose one direction for E_0 as shown in figure 1b and then the amplitude of the unpolarized beam is summed over all directions. A force is exerted on the electron which produces

$$a_Y = \frac{f_Y}{m} = \frac{eE_{0Y}}{m}\sin 2\pi\upsilon t \qquad a_Z = \frac{f_Z}{m} = \frac{eE_{0Z}}{m}\sin 2\pi\upsilon t$$

Using (1.1), we have

$$E_{Y'} = \frac{e^2 E_{OY}}{mc^2 R}\cos\phi \qquad E_{Z'} = \frac{e^2 E_{0Z}}{mc^2 R}$$

where the relation between ε and E is that

$$\varepsilon_{OY} = E_{OY}\sin 2\pi\upsilon t \qquad \varepsilon_{Y'} = E_{Y'}\sin 2\pi\upsilon t$$
$$\varepsilon_{OZ} = E_{OZ}\sin 2\pi\upsilon t \qquad \varepsilon_{Z'} = E_{Z'}\sin 2\pi\upsilon t$$

The resultant amplitude E at the point of observation is given by

$$E^2 = E_{Z'}^2 + E_{Y'}^2 = \frac{e^4}{m^2 c^4 R^2}(E_{OZ}^2 + E_{OY}^2\cos^2\phi)$$

Since the incident radiation vector lies in any orientation in the YZ-plane with equal probability, the Y-axis and Z-axis are equivalent and

$$< E_{0Y}^2 >=< E_{0Z}^2 >= \frac{1}{2} < E_0^2 >$$

and

$$< E^2 >=< E_0^2 > \frac{e^4}{m^2 c^4 R^2}(\frac{1+\cos^2\phi}{2})$$

The intensity I is proportional to $<E^2>$, and the scattered radiation intensity is given by

$$I = I_0 \frac{e^4}{m^2 c^4 R^2} \left(\frac{1+\cos^2\phi}{2}\right) \qquad (1.2)$$

and $(1+\cos^2\phi)/2$ is called the polarization factor.

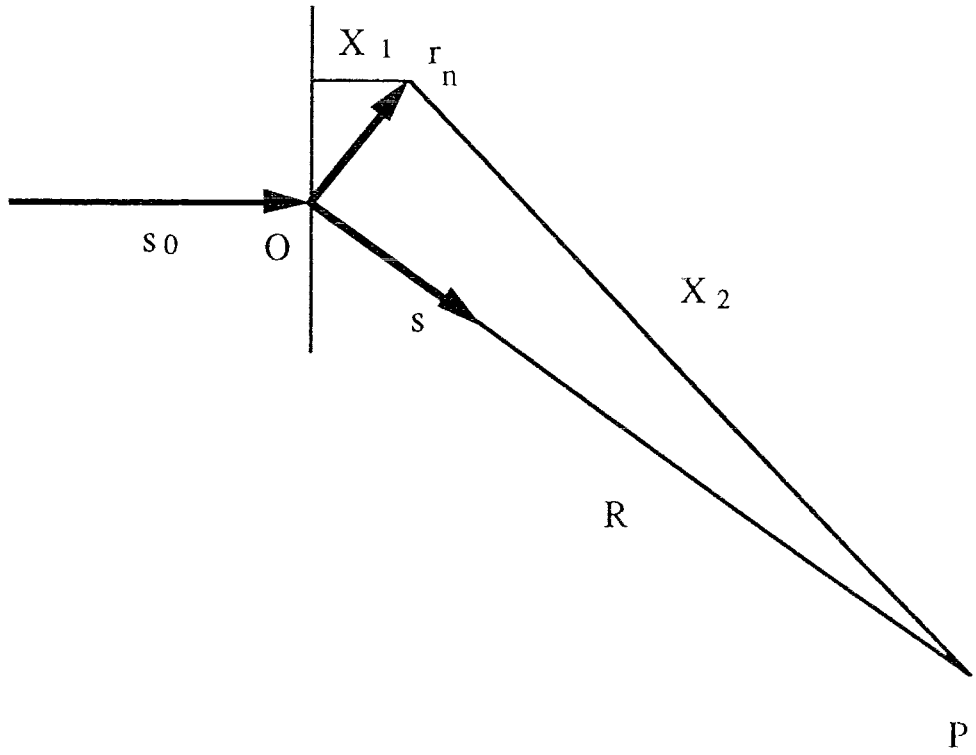

Figure 1c Scattering by a group of electrons at point $\mathbf{r_n}$.

The wave length of the diffracted X-ray is comparable to the size of an atom. The phase difference from different parts of an atom must be considered. Figure 1c shows the scattering by a group of electrons. At position $\mathbf{r_n}$, $\mathbf{s_0}$ and $\mathbf{s}$ are the unit vectors of the direction of the primary beam and the direction of the point of observation *P* respectively. In terms of a wave front through *O*, the instantaneous value of the field at point $\mathbf{r_n}$ is given by:

$$\varepsilon_0 = E_0 \cos(2\pi\upsilon t - \frac{2\pi X_1}{\lambda})$$

The total path is X_1+X_2 , the magnitude and phase of the scattered beam at P due to electron n, is

$$\varepsilon_0 = \frac{E_0 e^2}{mc^2 X_2}\cos[2\pi\upsilon t - \frac{2\pi}{\lambda}(X_1 + X_2)]$$

Here a 180° jump in phase in the scattering is dropped: it doesn't affect the final results since it is the same for all the electrons. Using the usual plane-wave approximations with X_2 --->R , we get

$$X_1 + X_2 = \mathbf{r_n}\cdot\mathbf{s_n} + R - \mathbf{r_n}\cdot\mathbf{s} = R - (\mathbf{s}-\mathbf{s_n})\cdot\mathbf{r_n}$$

In terms of the complex exponential, the sum of the instantaneous fields at P is given by

$$\varepsilon = \frac{E_0 e^2}{mc^2} e^{2\pi i[\upsilon t-(R/\lambda)]}\sum_n e^{(2\pi i/\lambda)(\mathbf{s}-\mathbf{s_0})\cdot\mathbf{r_n}}$$

where the sum over n is for all the electrons in the atom.

If each electron is spread out into a diffuse cloud of negative charge.

$$\varepsilon_0 = \frac{E_0 e^2}{mc^2 R} e^{2\pi i[\upsilon t-(R/\lambda)]}\sum_n \int e^{(2\pi i/\lambda)(\mathbf{s}-\mathbf{s_0})\cdot\mathbf{r_n}}\rho_n dV$$

where ρ_n is a charge density for electron n in space. The scattering factor per electron is given by

$$f_e = \int e^{(2\pi i/\lambda)(\mathbf{s}-\mathbf{s_0})\cdot\mathbf{r}}\rho dV$$

If the charge distribution has spherical symmetry for each electron in an atom, the scattering factor for the atom with several electrons is

$$f = \sum_n \int_0^\infty 4\pi r^2 \rho_n(r)\frac{\sin kr}{kr}dr \qquad (1.3)$$

If we consider the intensity scattered by a small crystal, intense peaks occur only when the Bragg law is satisfied. Since the planes of a given Miller index are spaced on the order of the wavelength of the X-ray, the phase difference from scattered X-rays from the planes must be considered. The structure factor is defined as

$$F_{hkl} = \sum_n f_n e^{2\pi i(hx_n + ky_n + lz_n)} \qquad (1.4)$$

where h, k, l are Miller indices and x_n, y_n, z_n are the fractional coordinates. This structure factor does not include thermal vibration parameters.

In powder X-ray diffraction, the ideal powder consists of an enormous number of very tiny crystals of size 10^{-3}cm or smaller with totally random orientation. These samples can be obtained as fine grained precipitates [43], or by grinding coarse crystalline material, or by making filings in the case of metals. Here we use $Li_xNi_{2-x}O_2$ powder ground with pestle and mortar.

For a powder sample, the large number of small crystals is distributed in all orientations with the same probability. Thus, there is a number of orientations for a small crystal in which X-ray scattering can satisfy the Bragg condition at the same Bragg angle; these orientations correspond to a certain Miller index, and the number of orientations is the multiplicity.

X-ray diffraction measurements were made using a Phillips powder diffractometer. The radiation used for the powder method is the CuK $\alpha_1\alpha_2$ doublet, where λ_1=1.54056Å and λ_2=1.54404Å.

The diffractometer is illustrated in figure 1d. The sample is a flat-faced slab of powder. Monochromatic radiation from the source goes through the

entrance slit E, and strikes the sample. The diffracted radiation is selected by the detector through a narrow receiving slit R. The distances EO and OR are made equal, and the sample face is maintained symmetrical with respect to the primary and diffracted beams. The pulses produced in the detector are amplified and fed to a computer. During the measurement the detector is fixed at a particular angle for some time, and there is no measurement while the angle is changed. The sample face is kept symmetrical with respect to the primary and diffracted beams because the detector turns at an angle 2θ while the sample turns at angle θ.

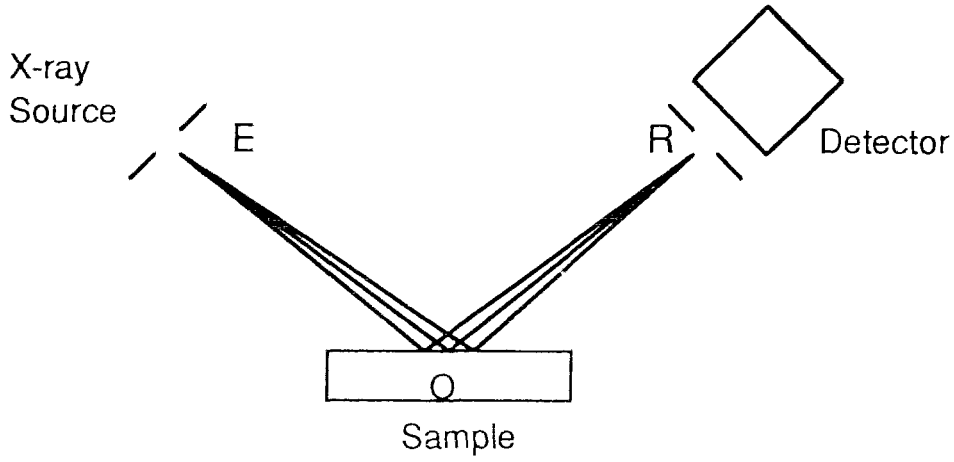

Figure 1d X-ray diffraction patterns in powders are recorded by the counter diffractometer

For powder patterns recorded by a powder diffractometer, the handling of the systematic error can be complex. There are systematic errors even with a well-built diffractometer having a very accurately graduated scale. They usually result from three effects:

1. The beam penetrates below the sample surface.

2. There is a zero error in the setting of the 2θ.

3. Axial divergence error occurs.

Error 1 is of importance for samples with low absorption coefficients, but $Li_xNi_{2-x}O_2$ is not this case. Error 2 is solved by adjusting the zero point in the Rietveld fitting program [44]. Error 3 consists of two parts. One is a constant term $\Delta d/d=h^2/(8R^2)$, where d is the distance of diffracting planes, R is the distance of OR in figure 1.3, and$h$ is the size of the entrance slit. The other is relative to $\cos^2\theta$ and it can be eliminated by a $\cos^2\theta$ extrapolation. The constant term $h^2/(8R^2)$ is about 10^{-6} and it implies an error $\Delta d/d$ about the same order.

Thermal vibration affects X-ray diffraction. The most familiar effect of thermal vibration is the reduction of the intensities of the crystalline reflections by the Debye temperature factor exp[-2M]. It gives a method for obtaining the mean square amplitudes of vibration of the atoms $<\mu_s^2>$. Since it weakens the reflections that we desire to measure, we must correct for it in crystal structure determinations where quantitative values of the structure factor are necessary. It is easy to understand that vibrations produce a diffuse intensity and reduce the intensities of the crystalline reflections. The intensities are reduced by a factor exp[-2M] for a crystal containing only one kind of atom. For the general crystal containing more than one kind of atom, one replaces each f_n in the structure factor by $f_n\exp[-M_n]$. The factor, M_n is given by

$$M_n=8\pi^2<\mu_s^2>_n (\sin^2\theta)/\lambda^2$$

where $\langle \mu_s^2 \rangle$ is the mean square component of displacement of atom n normal to the reflecting planes. For simple structures, the value of the factor exp[-2M] can be obtained directly from the measured integrated intensities, and the corresponding values of the root mean square components of displacement $\langle \mu_s^2 \rangle^{1/2}$.

4. Structure and Order Parameter

The compounds $Li_xNi_{2-x}O_2$ are structurally related to NiO which has a rock-salt structure with a_c=4.168 Å. In this structure, the metal ions occupy one Face-Centered Cubic (FCC) frame while the oxygen ions occupy the other FCC frame. These two FCC frames are shifted by $a_c/2$ along one of the three cube axes. For $0.0 \le x \le 0.62$ $Li_xNi_{2-x}O_2$ is cubic and for $0.62 \le x \le 1.0$ it is hexagonal. Fig. 2(a) shows the metal atom positions when x=1 and c_h and a_h are cell constants in the hexagonal structure. When $c_h/a_h = 2\sqrt{6}$ the unit cell is equivalent to cubic one with $a_c = \sqrt{2}\, a_h$.

As figure 2a shows, the metal atoms segregate into predominantly Li filled layers (L layers) and predominantly Ni filled layers (N layers) near x=1. As x in $Li_xNi_{2-x}O_2$ decreases, Ni atoms must move into the L layers and Li atoms may move into N layers. We define a long-range order parameter as

$$\eta = | \langle x_L \rangle - \langle x_N \rangle | \qquad (2.1)$$

where

$$\langle x_L \rangle + \langle x_N \rangle = x \qquad (2.2)$$

and where $\langle x_L \rangle$ and $\langle x_N \rangle$ are the average Li concentrations in the L layers and N layers respectively. In figure 2a, η=1 since the structure is perfectly ordered. Figure 2b shows a situation for x<1 where the lattice is partially

ordered and has $\eta<1$. Finally, figure 2c shows the cation positions in NiO which has $\eta=0$ according to our definition.

Profile refinements are methods that minimize the difference between experimental and calculated intensities to obtain structural information. In our profile refinements, we refine the concentrations x_L and x_N. In an L layer each site is filled by an average atom consisting of x_L Li and (1 - x_L) Ni. In an N layer, each site is filled by x_N Li and (1 - x_N) Ni. Since lithium has only three electrons, we are most sensitive to lithium through the absence of Ni, since we assume the number of cations in the structure equals the number of oxygen atoms.

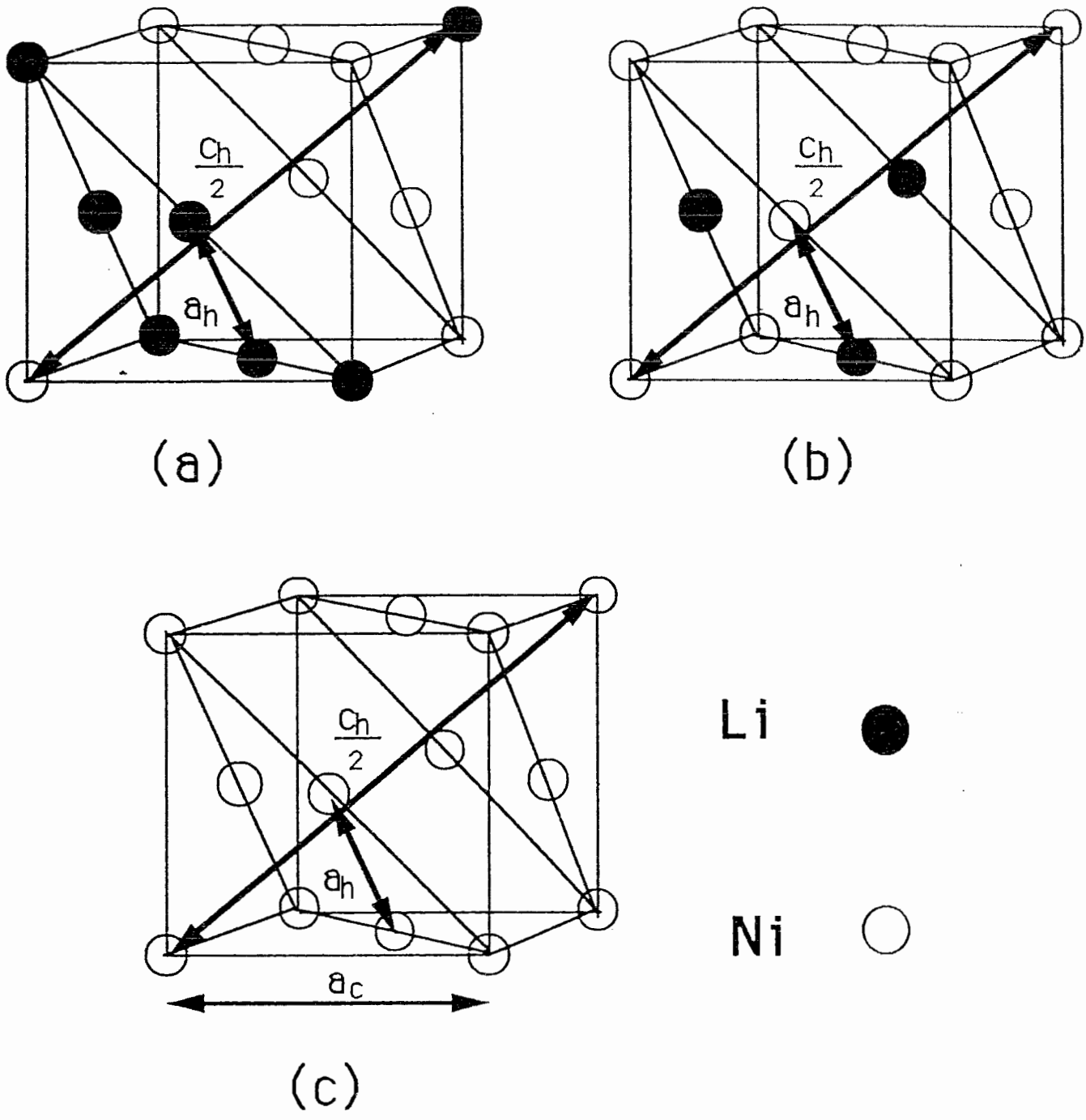

Fig. 2 Metal Positions in $Li_xNi_{2-x}O_2$

(a) x=1.0 and η=1.0, $LiNiO_2$ with the perfect ordered structure.

(b) $0<x<1$, and $0<\eta<1$ with the partial ordered structure

(c) x=0.0 and η=0.0, NiO

5. Refinement Results

5.1 Rietveld refinement method

The Rietveld structure refinement procedure was first introduced in 1966 [45]. The method is widely used in X-ray and neutron diffraction. It is for crystal structure refinement which does not use integrated powder diffraction intensities, but employs directly the profile intensities obtained from step-scanning measurements of the powder diagram. Fourier techniques assist the Rietveld method when used in the *ab initio* solution of crystal structures from powder diffraction data.

The first program in Rietveld method was written specifically for the analysis of neutron diffraction data from fixed-wavelength diffractometers by Rietveld [1969]. It was developed further by Hewat [1973] and used successfully by a number of other workers. The method has been extended to the refinement of neutron patterns recorded with time-of-flight diffractometers. The program for the analysis of X-ray data appeared in 1977, and a more advanced program was used to solve crystal structure problems subject to quite sophisticated constraints.

The program for the Rietveld refinement was described by Wiles and Young [46] in analysis both for X-ray and neutron diffraction patterns recorded with conventional (fixed wavelength) diffractometers. The structures of two coexisting phases can be refined with this program which also accommodates data recorded for two wavelengths (such as the X-ray doublet). The background can be refined or prescribed in the program as required. There is a built-in table of X-ray scattering factors, and neutron nuclear scattering lengths , and calculation of symmetry operators from a standard space-group symbol for easy use. The new program [44] called LHPM1 was developed by R. J. Hill and C. J. Howard and is used here to analyze the X-ray data.

The basis for the Rietveld method [44] is the equation

$$Y_{ic} = Y_{ib} + \sum_k G_{ik} I_k \qquad (3)$$

where Y_{ic} is the net intensity calculated at point i in the pattern and Y_{ib} is the background intensity. In our calculation, Y_{ib} was chosen as $A+B\theta+C/\theta$ and A, B, C are profile parameters. G_{ik} is a normalized peak profile function. I_k is the intensity of the k^{th} Bragg reflection and k is summed over all reflections contributing to the intensity at point i.

Based on the introduction of Chapter 3, , we give the expression of intensity I_k.

$$I_k = S M_k L_k |F_k|^2 W_k \qquad (4)$$

where S is the usual scale factor, M_k is the multiplicity, L_k is the Lorentz polarization factor, W_k is an isotropic Debye-Waller factor which we have

assumed is the same for each atom in the unit cell, and F_k is the structure factor

$$F_k = \sum_{j=1}^{n} f_j \exp[2\pi i h_k r_j] \qquad (5)$$

where f_j is the scattering factor of atom j, and h_k, r_j are matrices representing the Miller indices, and atomic coordinates respectively.

The ratio of the intensities for the two wavelengths comes directly from quantum mechanics and is equal to 1/2, so that only a single scale factor is required. The peak profile function G_{ik} is chosen as the pseudo-Voigt function

$$G_{ik} = \gamma \frac{C_0^{1/2}}{H_k \pi} [1 + C_0 X_{ik}^2]^{-1} + (1-\gamma) \frac{C_1^{1/2}}{H_k \pi^{1/2}} \exp[-C_1 X_{ik}^2] \qquad (6.1)$$

where $C_0=4$, $C_1=4\ln 2$, H_k is the full-width at half-maximum (FWHM) of the k^{th} Bragg reflection, $X_{ik}=(2\theta_i-2\theta_k)/H_k$, and γ is a refinable 'mixing' parameter.

The pseudo-Voigt function can be assigned a fixed shape of any type between its limiting Gaussian and Lorentzian forms (γ=0 and 1 respectively for the pseudo-Voigt). The peak shape can be varied across the pattern by application of the function

$$\gamma=\gamma_1+\gamma_2 2\theta+\gamma_3(2\theta)^2 \qquad (6.2)$$

where γ_1, γ_2, γ_3 are refinable parameters.

For this profile type, the variation of the peak FWHM is defined by the function described by Gaglioti *et al.* [47].

$$H_k=(U\tan^2\theta+V\tan\theta+W)^{1/2} \qquad (6.3)$$

where U, V and W are refinable parameters.

The least-squares procedure uses the Newton-Raphson algorithm to minimize the quantity

$$R=\sum_i w_i(Y_{io}-Y_{ic})^2 \qquad (7.1)$$

where Y_{io} is the set of observed diffraction intensities collected at each step across the pattern, Y_{ic} is the set of corresponding calculated values obtained from equation (3), and w_i is the statistical weight assigned to each observation. The minimisation of R is undertaken over all data points contributing to the peaks and the background. The weight w_i assigned to each observation was $w_i=\sqrt{Y_{io}}$.

The quantities used to estimate the agreement between the observations and the model during the course of the refinement are as follows:

(i) The profile R factor, R_p,

$$R_p=\frac{\sum|Y_{io}-Y_{ic}|}{\sum Y_{io}} \qquad (7.2)$$

(i) The weighted profile R factor, R_{wp},

$$R_{wp}=\left[\frac{\sum w_i(Y_{io}-Y_{ic})^2}{\sum w_i Y_{io}^2}\right]^{1/2} \qquad (7.3)$$

and (i) The Bragg R factor, R_B

$$R_B=\frac{\sum|I_{ko}-I_{kc}|}{\sum I_{kc}} \qquad (7.4)$$

where I_{ko} is the 'observed' integrated intensity of reflection k calculated at the end of refinement after apportioning each Y_{io} between the contributing peaks and background according to the calculated intensities I_{kc}.

In the Rietveld refinement, the values for the X-ray radiation wavelengths are λ_1=1.54056Å and λ_2=1.54440Å, and the intensity ratio of λ_1 and λ_2 is exactly 0.5. The width (range) of calculated profile (in units of H_k) beyond which it is set to zero was 3. The coefficient in formula for polarization correction is 0.808 due to diffracted beam monochromator. The individual isotropic temperature factor and anisotropic temperature factors were not used. Only an overall isotropic temperature factor was included in the refinement. The number of parameters was between 10 to 15 and the number of the data points was between 1400 to 1900.

5.2 X-ray Refinement Results

Figure 3 shows X-ray diffraction profiles for several $Li_xNi_{2-x}O_2$ samples, to show the changes in the profile which occur as x changes. The $(003)_H$ peak decreases in intensity as x decreases, becoming weak and broad below x=0.62, indicating short-range instead of long-range correlations. The sharp peak appears only when the average composition of the L and N layers differs. The ratio of the intensities of the $(101)_H$ and the $(102)_H$, $(006)_H$ peaks changes with x and has been previously used to estimate x in $Li_xNi_{2-x}O_2$ [28].

Figure 4a shows an example of a Rietveld profile refinement for one of our samples. For x>0.62, the fits included at least 12 Bragg peaks while for x<0.62

only 6 (including 2 peaks between 80° and 100° 2θ) experimentally measured peaks could be used. For x<0.62, the Rietveld program is unable to the fit the broad short-range order peak well near 2θ =18.5°, because its width does not follow the functional form used by the Rietveld method. Nevertheless, we refined the entire profile and considered the short-range order peak separately as we describe later. Figure 4b shows the Rietveld profile refinement with $x=0.667$ which is above the order-disorder structure transition, the peak near 2θ=18.5°is fit well. Figure 4c shows the results with $x=0.55$ just below the order-disorder transition, the peak near 2θ=18.5° becomes broad and the calculated peak can not follow its width. Figure 4d shows the results with $x=0.45$ which is in the disordered phase far from the transition point; the peak near 2θ=18.5° in experiment is very broad and weak, the calculated peak is weak too but the width is narrow. Table 1 reports the results of our refinements. For all refinements, R_B, was less than 3.4%, indicating good agreement between the data and the structural model.

The composition of the samples are determined in two ways. First we simply use the mole ratios of the starting materials mixed in the synthesis. The Rietveld program gave a second value for x, obtained by summing the x_N and x_L returned by the program. We call the first composition "x from synthesis" and the second "x from Rietveld profile fitting". Figure 5 shows that these compositions agree well with each other, which gives us confidence both in the quality of our samples and the refinement method. The solid line in figure 5 shows the line "x from synthesis"="x from Rietveld profile fitting". Apart from 2 points, our data fall systematically to one side of the line suggesting some small problem with our refinement methods or in the original stoichiometries of our starting materials. In what follows, we plot

refined quantities versus "x from Rietveld profile fitting" for consistency. Substituting "x from synthesis" does not change the results significantly.

All Rietveld profile fitting is based on the hexagonal structure, even if the structure could be fitted by a cubic structure for $0.0<x<0.62$ (The $(003)_H$ peak will disppear in calculation if it is fitted by a cubic structure while the broad and weak $(003)_H$ peak exists in experiment). The cell constants a_h and c_h in figure 7 and figure 6 are in good agreement with the data given by other workers [31, 28]. For $x<0.62$ in the cubic structure, the refined x differ by less than 0.03 between the cubic and the hexagonal structure used in the Rietveld profile fitting. Figure 8 shows $\sqrt{24}\ a_h/c_h$ from Rietveld profile fitting in the hexagonal structure, for $0\leq x\leq 1$. When $\sqrt{24}\ a_h/c_h=1$ the structure is cubic. The error bars are larger for $x<0.62$ than those for $0.62<x<1.0$, because fewer Bragg peaks are included in the refinements. In our estimate, the composition of the order-disorder transition is best obtained from figure 8. We measure $x_c=0.62$.

Figure 9 shows the order parameter η versus "x from synthesis". At $x=1$, full order is still not obtained since $\eta=0.96$; this means there are some Li atoms in Ni rich layers and some Ni atoms in Li rich layers even for stoichiometric $LiNiO_2$. This result agrees with that from recent neutron scattering measurements on $LiNiO_2$ [55]. For $x<0.62$, there is still short-range order as evidenced by the weak and broad peak in the $(003)_H$ position. Our Rietveld refinements are all done in the hexagonal system and do not treat the short range order peak well. The refinement gives non-zero long range order parameters below $x_c=0.62$ in an attempt to fit the weak broad peak. We have sketched a guide to the eye in figure 9 which indicates how the long range order parameter must behave. We have indicated with squares, those fitting

results which are an artifact of our procedure and not indicative of true long-range order. More careful fitting of the critical scattering is needed to fully understand the short-range order.

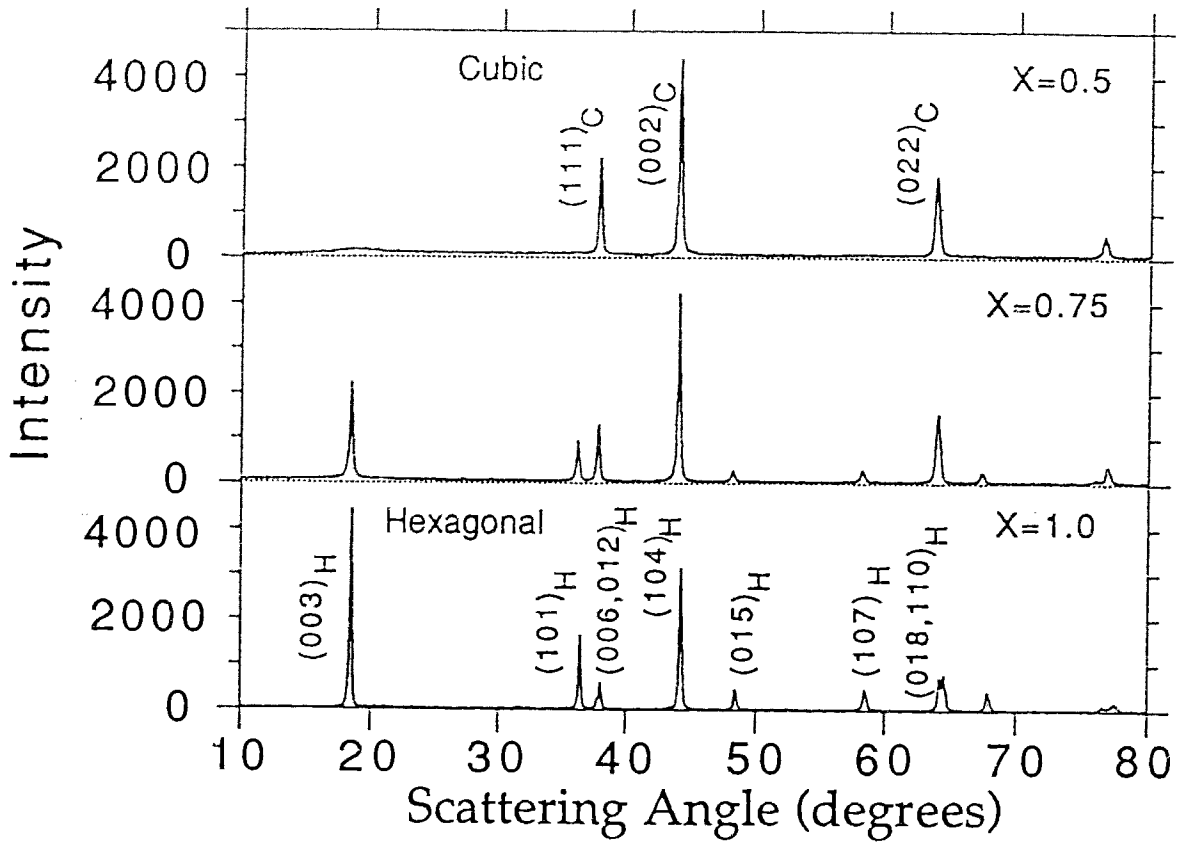

Fig. 3 X-ray diffraction patterns for three $Li_xNi_{2-x}O_2$ samples with x as indicated in the figure. Miller indices for Bragg peaks referred to in the text are indicated.

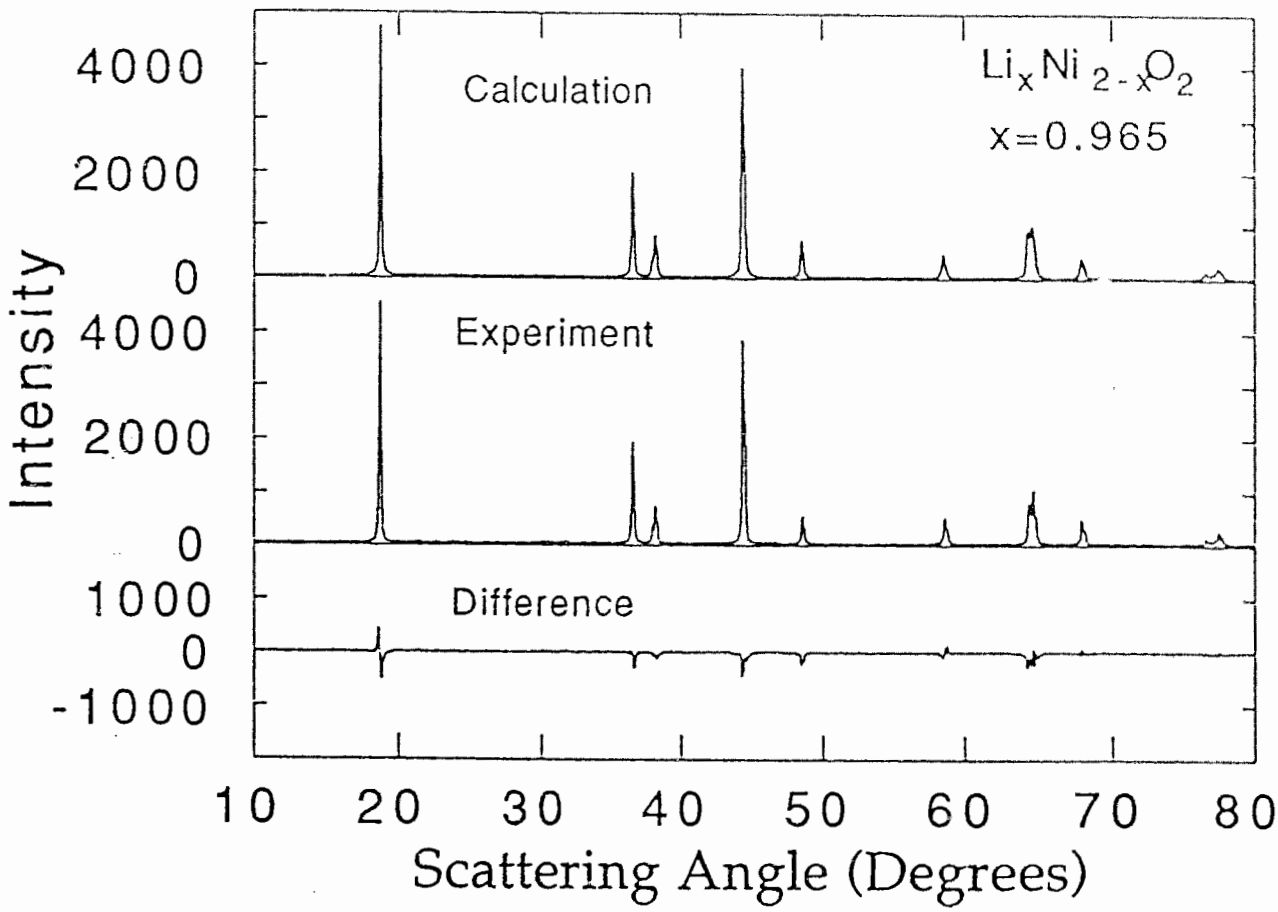

Figure 4a Experiment and fitted profile for $Li_{0.965}Ni_{1.035}O_2$ as indicated in the figure. The difference between the two profiles is also shown.

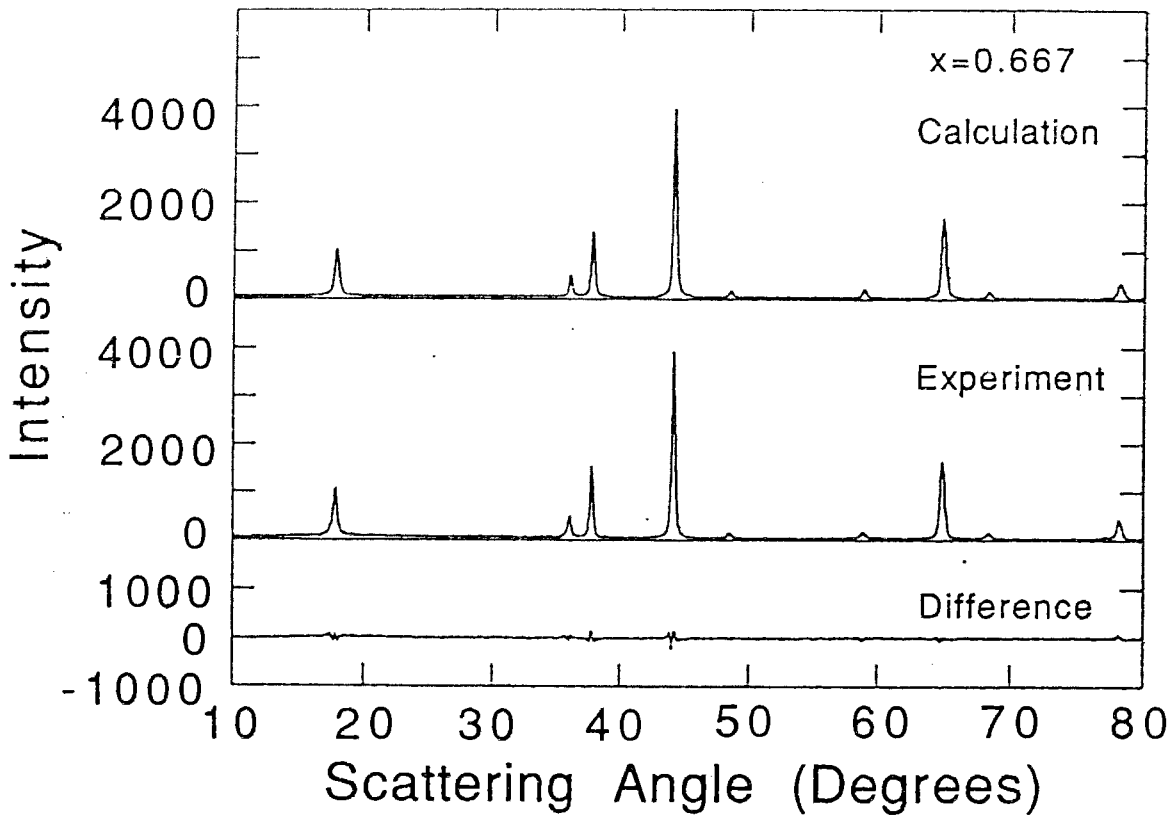

Figure 4b Experiment and fitted profile for $Li_{0.667}Ni_{1.333}O_2$ as indicated in the figure. This sample is in the ordered phase.

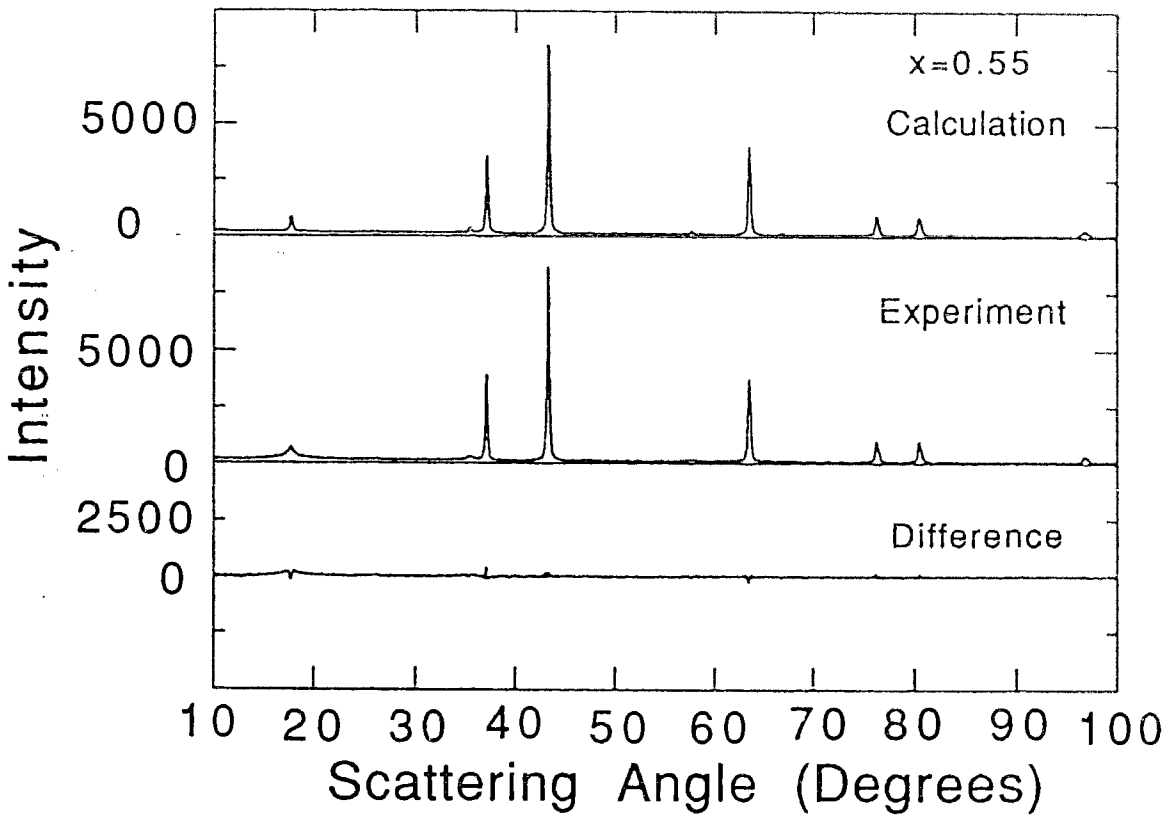

Figure 4c Experiment and fitted profile for $Li_{0.55}Ni_{1.45}O_2$ as indicated in the figure. This sample is in the disordered phase.

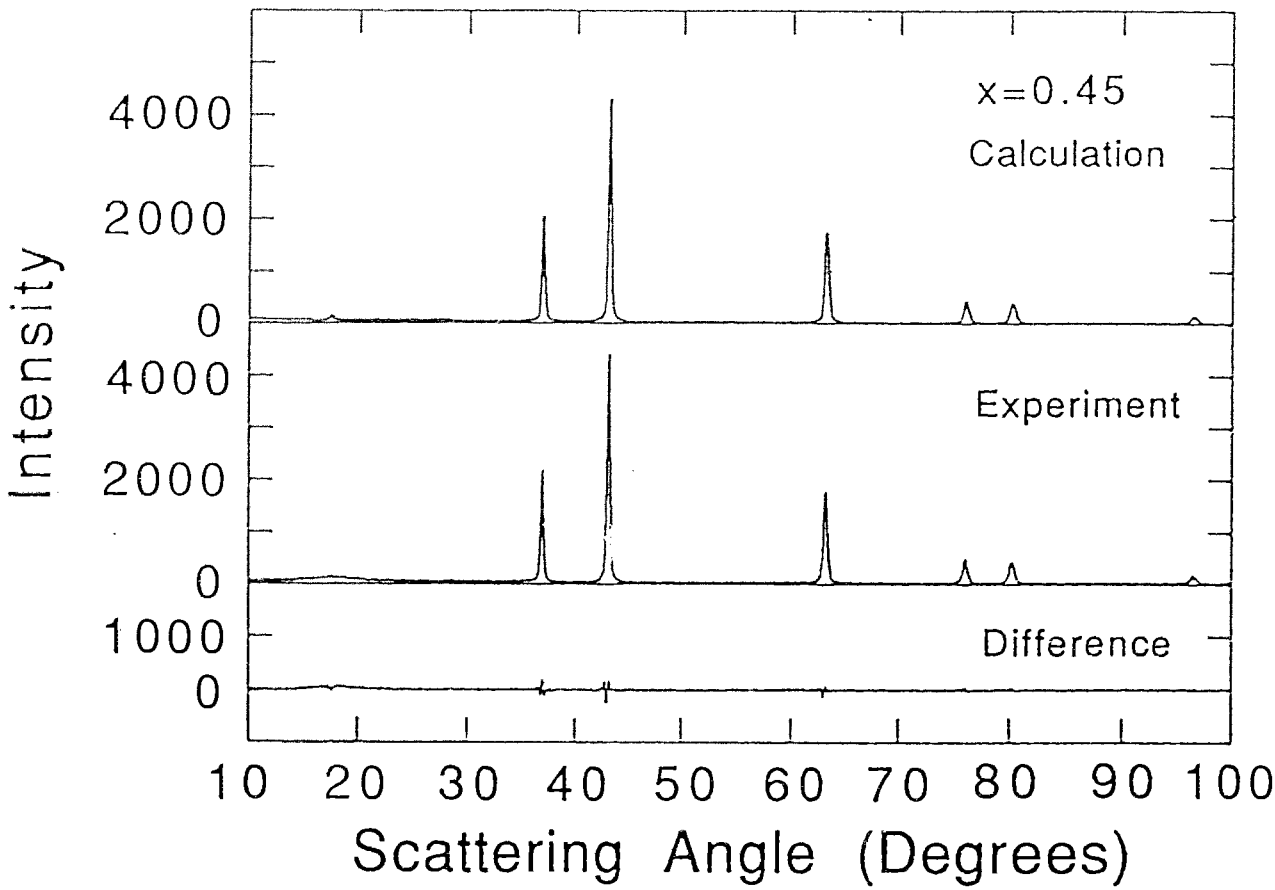

Figure 4d Experiment and fitted profile for $Li_{0.45}Ni_{1.55}O_2$ as indicated in the figure. This sample is in the disordered phase.

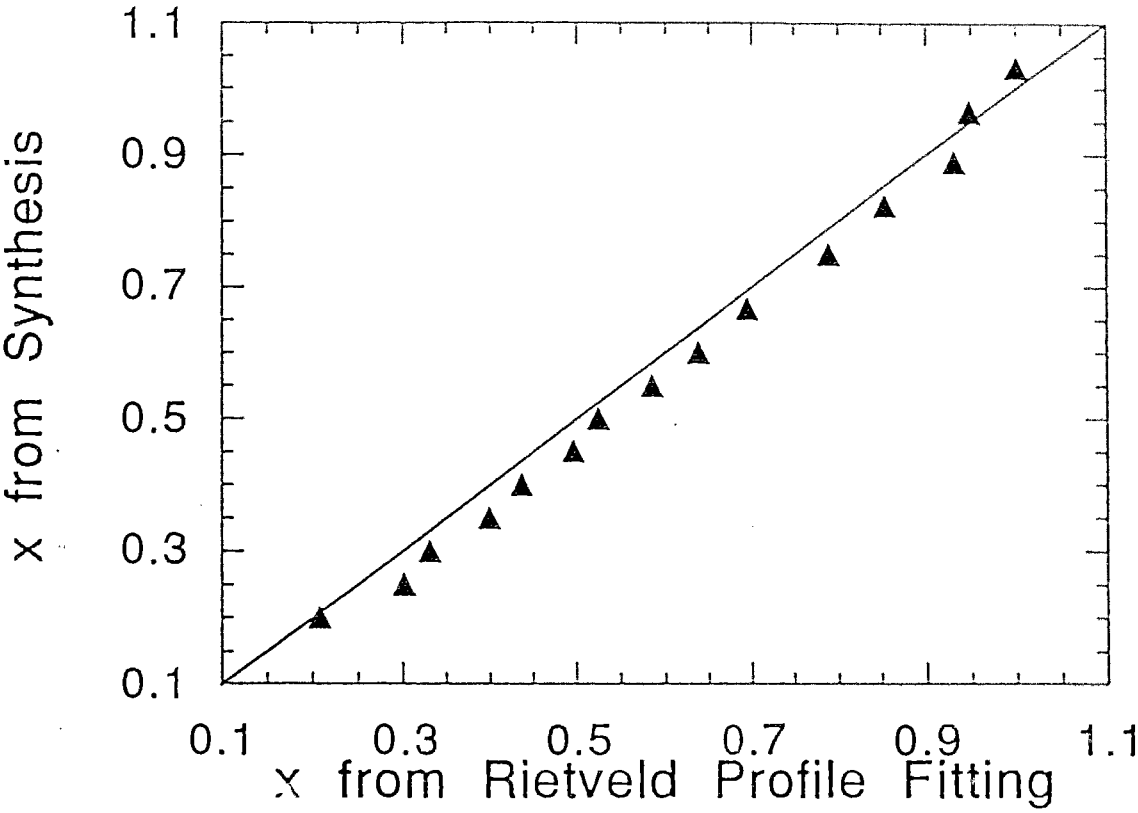

Figure 5 The composition of $Li_xNi_{2-x}O_2$ measured from mole ratios of reactants ("x from synthesis") plotted versus the composition determined from Rietveld profile analysis ("x from Rietveld profile fitting"). The solid line is "x from synthesis"="x from Rietveld profile analysis"

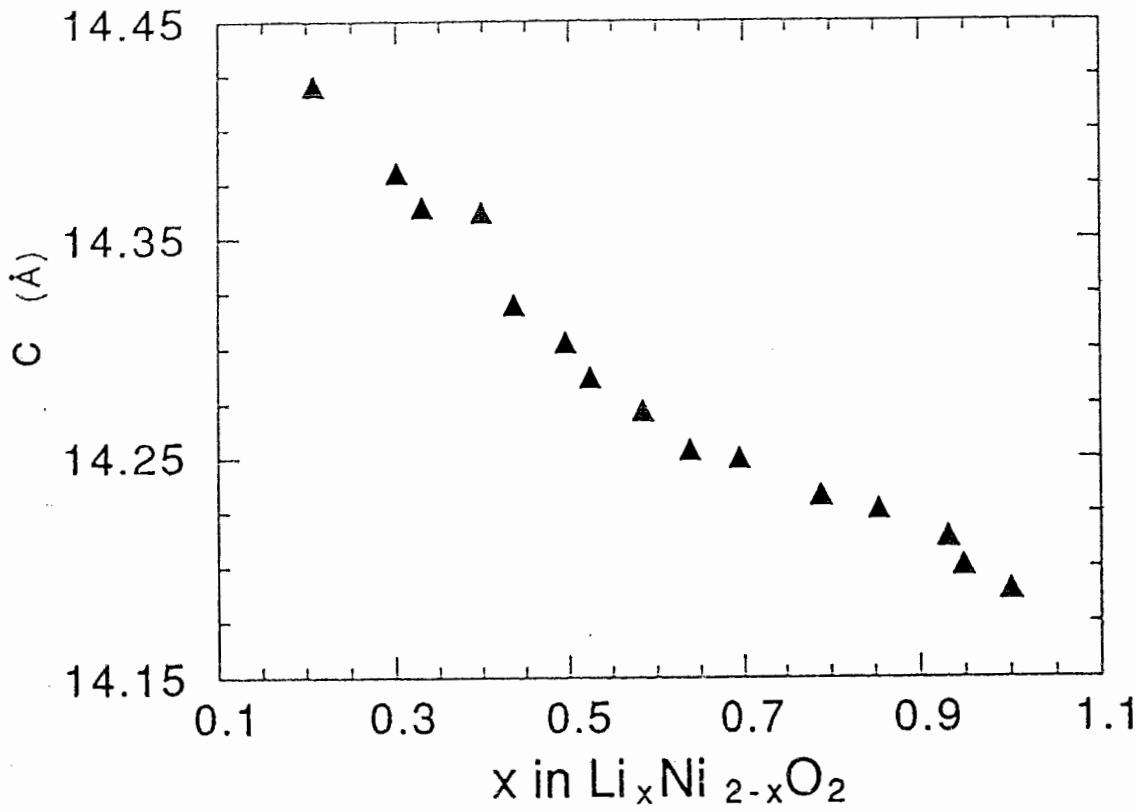

Fig. 6 The cell constant, c_h, of the hexagonal structure vs. "x from Rietveld profile fitting" in $Li_xNi_{2-x}O_2$.

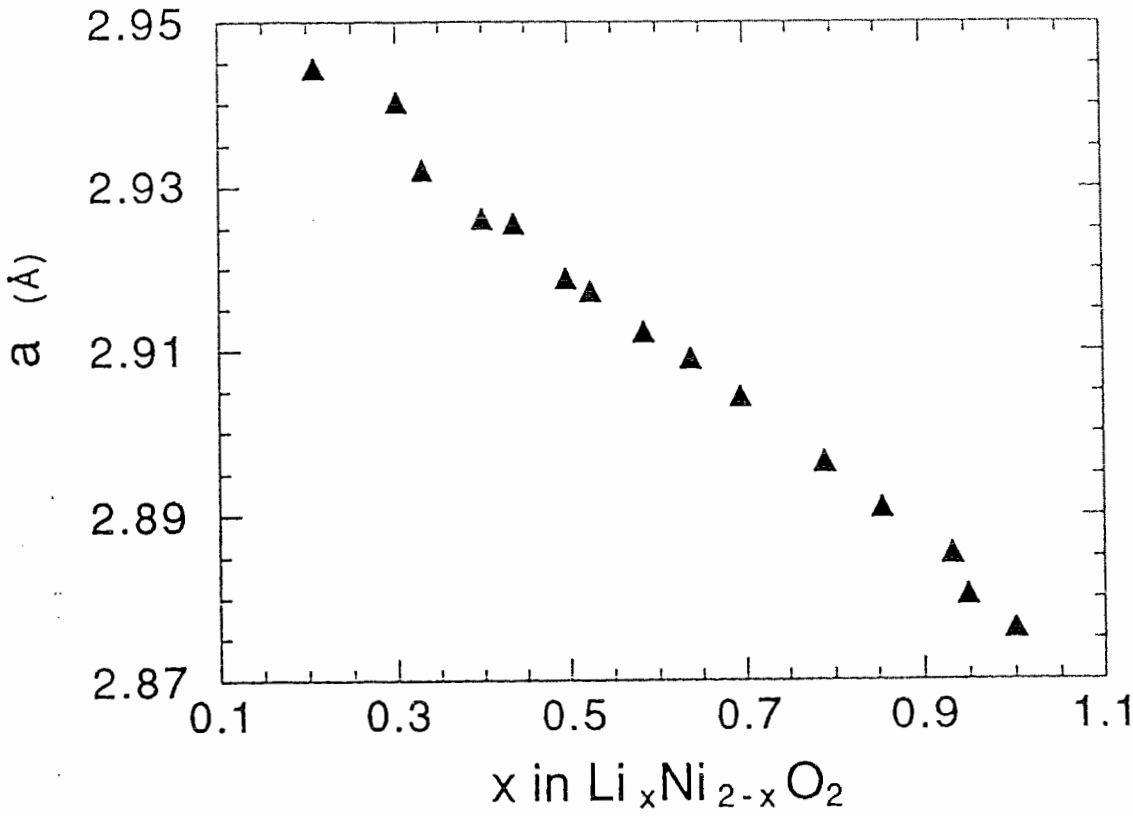

Fig. 7 The cell constant, a_h of the hexagonal structure vs. "x from Rietveld profile fitting" in $Li_xNi_{2-x}O_2$

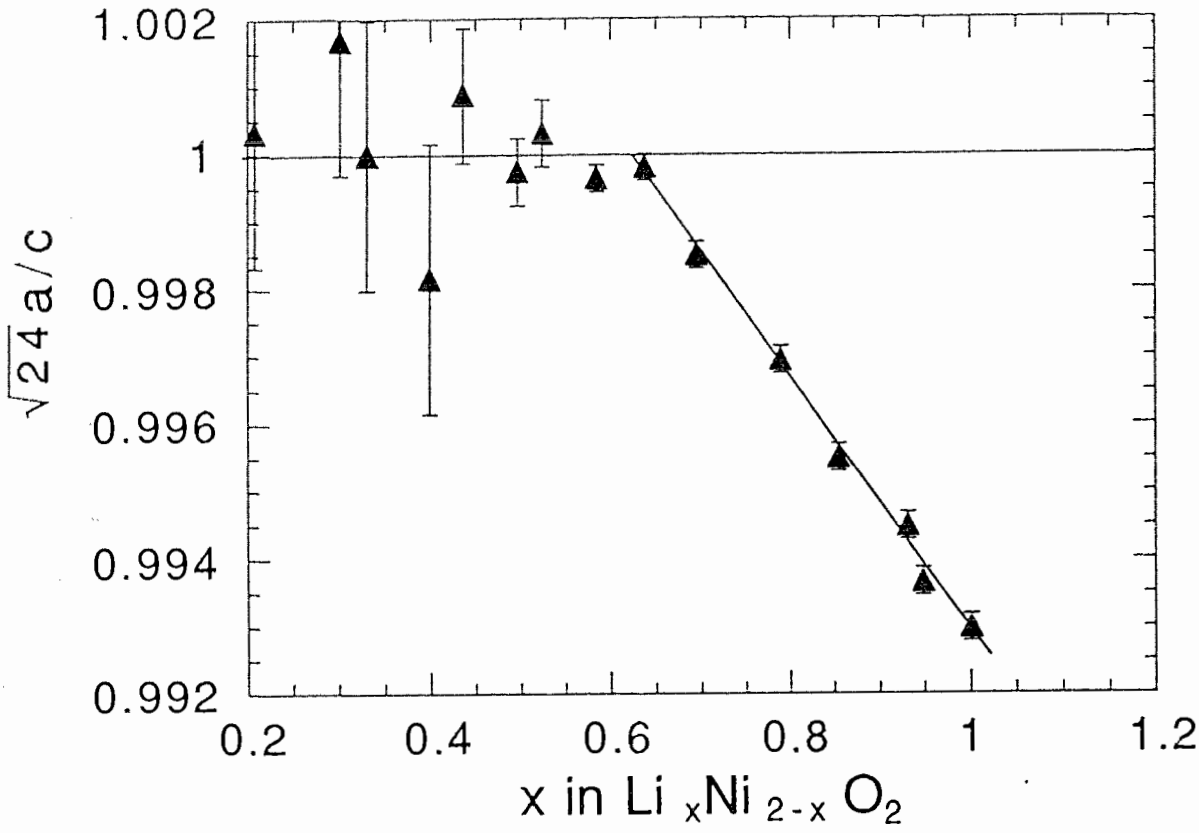

Fig. 8 The ratio a_h/c_h multiplied by $\sqrt{24}$ vs "x from Rietveld profile fitting". The structure is cubic for $\sqrt{24}a_h/c_h=1$.

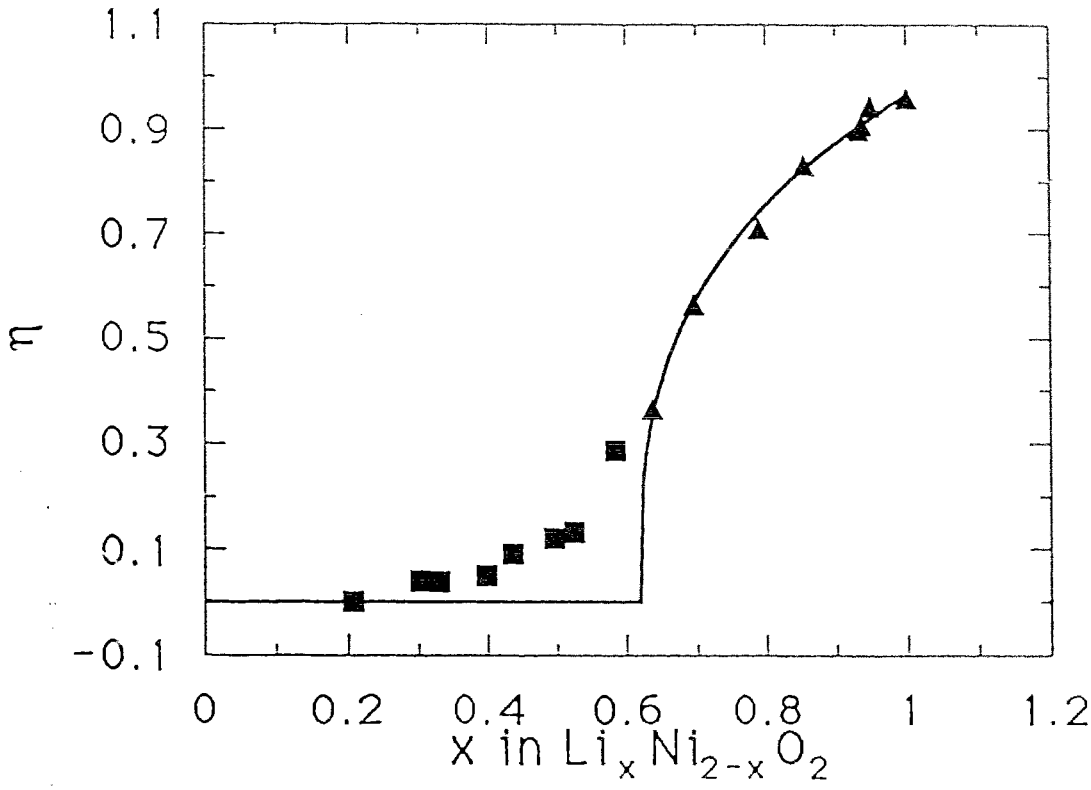

Fig. 9 The long range order parameter from Rietveld profile fitting vs. "x from Rietveld profile fitting". For x<0.62, the data do not indicate long range order (see text). The solid line is a guide to the eye.

Table 1 Results of Profile Refinement for $Li_xNi_{2-x}O_2$ Samples

Sample No	x^*	x^{**}	a_h (Å)	c_h (Å)	O(z)(1)
1	1.032 (1)	1.001 (10)	2.8762 (1)	14.190 (1)	0.2581 (3)
2	0.965 (1)	0.949 (11)	2.8804 (1)	14.201 (1)	0.2559 (3)
3	0.889 (1)	0.932 (9)	2.8854 (1)	14.213 (1)	0.2579 (3)
4	0.824 (1)	0.855 (3)	2.8910 (2)	14.227 (2)	0.2571 (3)
5	0.750 (1)	0.790 (9)	2.8964 (2)	14.234 (2)	0.2568 (3)
6	0.667 (1)	0.695 (10)	2.9044 (1)	14.250 (1)	0.2571 (3)
7	0.600 (1)	0.638 (10)	2.9090 (4)	14.254 (4)	0.2573 (4)
8	0.550 (1)	0.585 (12)	2.9122 (5)	14.272 (4)	0.2560 (5)
9	0.500 (1)	0.524 (12)	2.9172 (5)	14.287 (5)	0.2554 (8)
10	0.450 (1)	0.496 (14)	2.9188 (6)	14.303 (6)	0.2538 (1)
11	0.400 (1)	0.436 (13)	2.9256 (8)	14.320 (7)	0.2561 (5)
12	0.350 (1)	0.399 (13)	2.9262 (13)	14.362 (13)	0.2553 (10)
13	0.300 (1)	0.331 (13)	2.9321 (10)	14.365 (8)	0.2547 (11)
14	0.250 (1)	0.301 (14)	2.9403 (5)	14.380 (5)	0.2542 (10)
15***	0.200 (1)	0.208 (11)	2.9444 (2)	14.424 (1)	cubic

(1) O(z) is the z component (parallel to c_h) of the oxygen fractional atomic coordinate.

Sample	XL	XN	η	Rwp	Rexp	RB
1	0.980 (9)	0.021 (3)	0.959	14.1	8.9	3.00
2	0.947 (9)	0.002 (6)	0.945	12.8	9.7	3.36
3	0.915 (3)	0.017 (8)	0.898	14.2	9.1	2.35
4	0.843 (3)	0.012 (1)	0.831	13.6	9.0	2.26
5	0.750 (4)	0.040 (8)	0.710	12.8	9.1	2.43
6	0.630 (4)	0.065 (9)	0.565	11.5	9.2	2.92
7	0.502 (5)	0.136 (9)	0.366	12.5	6.7	2.10
8	0.436 (6)	0.148 (10)	0.288	12.9	6.7	1.96
9	0.329 (6)	0.195 (10)	0.134	9.92	3.4	1.39
10	0.309 (8)	0.188 (11)	0.121	15.8	10.2	1.31
11	0.264 (7)	0.172 (11)	0.092	15.8	10.5	1.52
12	0.224 (6)	0.175 (11)	0.045	7.93	5.0	0.90
13	0.185 (7)	0.146 (11)	0.039	15.8	10.2	1.52
14	0.171 (7)	0.130 (12)	0.041	6.69	5.0	1.07
15	cubic	cubic	0	9.09	4.8	1.21

X* is from synthesis

X** is from Rietveld profile fitting (X=XL+XN) and η=XL-XN

***The sample is fit in cubic structure

R_B is defined in (6)

$R_{wp} = [\frac{\sum w_i(y_{io} - y_{ic})^2}{\sum w_i y_{io}^2}]^{\frac{1}{2}}$ and wi is the weight of peak.

$R_{exp} = [\frac{N-P}{\sum w_i y_{io}^2}]^{\frac{1}{2}}$ where N is the number of observations and P is the number of least-squares parameter being estimated.

6 Lattice Gas Model

The system $Li_xNi_{2-x}O_2$ consists of one FCC frame of oxygen and one FCC frame of metal cations. The octahedral interstitial sites of the oxygen lattice are where the cations can be positioned. At each site, either a Li atom or a Ni atom can be placed subject to the constraint that we have x Li and $(2-x)$ Ni atoms per formula unit. A lattice gas model is therefore appropriate for the treatment of this material. Interactions between metal atoms cause the ordered arrangement in the $(111)_C$ planes. Fig. 10 shows the structure of the metal frame. There are twelve nearest neighbors (checkerboard circles) and six next nearest neighbors (grey circles) for each site (black circles). All the six next nearest neighbors do not share the same $(111)_C$ plane with the site at the origin. However, six of the nearest neighbors share the same $(111)_C$ layer with the atom at the origin and the other six do not.

In the lattice-gas treatment [56] we assume interactions between pairs of metal cations occupying nearest neighbor (nn) and next nearest neighbor (nnn) sites and neglect longer ranged interactions. These are denoted J_1^{NN}, $J_1^{LN}=J_1^{NL}$, J_1^{LL} for Ni-Ni Ni-Li and Li-Li first neighbor interactions respectively. Next nearest neighbor interactions use the same notations, except the subscript 2 replaces the 1. The model Hamiltonian is [56] then

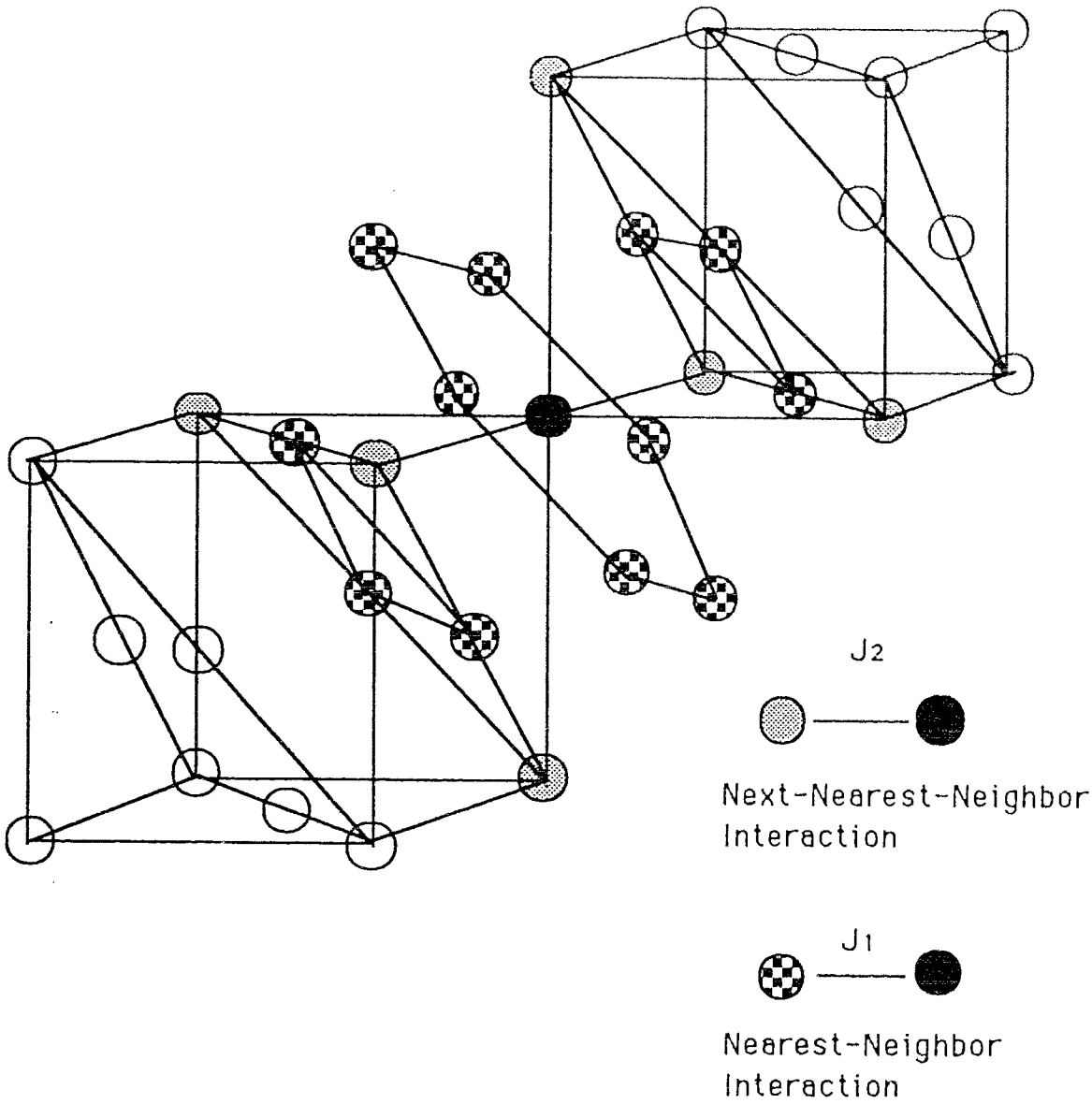

Figure 10 The cation FCC frame showing the nearest neighbor (checkerboard) and next-nearest neighbors (grey) to a particular site (black). The first and second neighbor interaction energies are shown.

$$H = \mu^L \sum_i x_i + \mu^N \sum_i y_i + \frac{1}{2}\sum_{i,j}^{NN} [J_1^{LL} x_i x_j + J_1^{LN} x_i y_j + J_1^{NL} y_i x_j + J_1^{NN} y_i y_j]$$
$$+ \frac{1}{2}\sum_{i,j}^{NNN} [J_2^{LL} x_i x_j + J_2^{LN} x_i y_j + J_2^{NL} y_i x_j + J_2^{NN} y_i y_j] \qquad (8.1)$$

Here, x_i =1 if site i is filled by Li and x_i =0 if site i not filled by Li. y_i =1 if site i is filled by Ni and y_i =0 if site i is filled by Ni. μ^N and μ^L are the chemical potentials for Li and Ni atoms respectively and the sums over the interaction terms run over all pairs of nearest neighbor atoms (the first term) and all pairs of next nearest neighbor atoms (the second term).

In our model we assume that all available sites are filled by either Li or Ni and that there are **no cation vacancies**. This allows considerable simplification of our Hamiltonian, since then y_i =1 - x_i. Making this substitution, we obtain

$$H = \sum_i \mu x_i + \frac{1}{2} J_1 \sum_{i,j}^{NN} x_i x_j + \frac{1}{2} J_2 \sum_{i,j}^{NNN} x_i x_j + N\mu^N + 6NJ_1^{NN} + 3NJ_2^{NN} \qquad (8.2)$$

where

$$\mu = \mu^L - \mu^N + 2(J_1^{LN} - J_1^{NN} + J_2^{LN} - J_2^{NN}),$$

$$J_1 = J_1^{LL} + J_1^{NN} - 2J_1^{LN}$$

and

$$J_2 = J_2^{LL} + J_2^{NN} - 2J_2^{LN}$$

Because we can redefine the zero of energy, we drop the constant terms $N\mu^N$ NJ_1^{NN} and NJ_2^{NN} in our subsequent analysis. Here, x_i is equal to 1 if a site is filled by Li and x_i =0 if it is not. Therefore, we have transformed the Hamiltonian from that commonly used for A-B alloys to that used for lattice-gas models in the usual fashion [48].

In order for the $(111)_C$ super-lattice ordering to be stabilized it turns out that one must have $J_2 \geq 0.5|J_1|$; for details the reader is refereed to reference [49]. For this case, a mean-field Bragg-Williams treatment of the problem is useful which we make below. In the Bragg-Williams model, we assume a superlattice structure commensurate with the ordered state. Assuming $(111)_C$ ordering, the Bragg-Williams Hamiltonian (8.4) is obtained by replacing the site occupancies x_i with $x+\eta/2$ and $x-\eta/2$ for sites on alternate $(111)_C$ cation planes. Here $x=\langle x_i \rangle$ is the average lithium concentration in the cation sites, equal to x in the compound $Li_xNi_{1-x}O$ and η is the order parameter defined earlier, in equation (2.1).

Dropping constant terms from (8.2) we have

$$H = \mu N x + \frac{1}{2} N J_1 [6(x-\frac{\eta}{2})(x+\frac{\eta}{2}) + 3(x+\frac{\eta}{2})^2 + 3(x-\frac{\eta}{2})^2]$$
$$+ \frac{1}{2} N J_2 [3(x+\frac{\eta}{2})^2 + 3(x-\frac{\eta}{2})^2] \qquad (8.3)$$

and we obtain the Bragg-Williams Hamiltonian

$$\frac{H}{N} = \mu x + 3(2J_1 + J_2)x^2 - \frac{3}{4} J_2 \eta^2 \qquad (8.4)$$

from which we can immediately see that the nearest neighbor interaction, J_1, does not couple to the order parameter in mean field theory. Figure 10 shows this as well; distributing 6 Li atoms randomly over the 12 nearest neighbors of a central Li atom "costs" $6J_1$ in energy, the same as if the atoms are in the ordered state, so we do not expect J_1 to couple to this ordered state. The order parameter η is actually four-fold degenerate corresponding to the four cubic directions; (111) $(1\ \bar{1}\ 1)$ $(1\ 1\ \bar{1})$ and $(1\ \bar{1}\ \bar{1})$ with order parameters η_1, η_2, η_3 and η_4, respectively.

Does the system select just one η or some linear combination of all four? To answer this question, we consider the relative entropies for these two situations. In mean-field theory, entropy is maximized in lattice gas arrangements with all site occupancies equal to one half, which is not possible in an ordered state with $\eta>0$. When $\eta\neq0$, entropy is maximized in ordered states where the *magnitude* of the deviation from half occupancy, is the same on each site. This certainly true for our ordered state where alternate (111) planes have average compositions $x+\eta/2$ and $x-\eta/2$. In an ordered state which is a mixture of the four (111) states, the magnitude or absolute value of the deviation of the average occupation from 1/2 will vary from site to site. Hence, the entropy is maximized in phases corresponding to one of the four possible (111) super-lattices and not in a mixture. A detailed proof [56] of this is given in appendix one.

The Bragg-Williams free energy is easily shown to be

$$\frac{F}{N}=\frac{H}{N}-\frac{TS}{N}$$

$$= \frac{H}{N} + \frac{k_B T}{2}[(x+\frac{\eta}{2})\ln(x+\frac{\eta}{2}) + (1-(x+\frac{\eta}{2}))\ln(1-(x+\frac{\eta}{2}))$$
$$+(x-\frac{\eta}{2})\ln(x-\frac{\eta}{2}) + (1-(x-\frac{\eta}{2}))\ln(1-(x-\frac{\eta}{2}))] \qquad (9.1)$$

Expanding in powers of η, we obtain

$$\frac{F}{N} = \mu x + 3(2J_1 + J_2)x^2 - \frac{3}{4}J_2\eta^2 + k_B T(x\ln x + (1-x)\ln(1-x))$$
$$+\frac{k_B T}{8}[\frac{1}{x} + \frac{1}{1-x}]\eta^2 + \frac{k_B T}{192}[\frac{1}{x^3} + \frac{1}{(1-x)^3}]\eta^4 + \ldots\ldots \qquad (9.2)$$

Using the Landau theory of phase transitions, we expect that F will be minimized for $\eta=0$ whenever

$$\frac{k_B T}{2}[\frac{1}{x} + \frac{1}{1-x}] - 3J_2 > 0 \qquad (9.3)$$

and that F will be minimized for $\eta>0$ whenever

$$\frac{k_B T}{2}[\frac{1}{x} + \frac{1}{1-x}] - 3J_2 < 0 \qquad (9.4)$$

This phase transition to $\eta\neq0$ occurs in the Bragg-Williams treatment when equality holds above, giving

$$x_c(1-x_c) = \frac{k_B T}{6J_2} \qquad (9.5)$$

where x_c is the critical lithium concentration in $Li_xNi_{1-x}O$ beyond which ordering in $(111)_C$ planes occurs. The data in Figure 8 show that the ordered state disappears for $x<x_c\approx0.62$ in $Li_xNi_{2-x}O_2$ which corresponds to $x_c=0.31$ in $Li_xNi_{1-x}O$. Substituting $x_c=0.31$ into the above equation gives

$$\frac{J_2}{k_BT}=0.78 \tag{9.6}$$

Rewriting the Bragg -Williams free energy given by equation (9.1) as

$$\begin{aligned}\frac{F}{N}&=\frac{H}{N}+\frac{1}{2}k_BT[x_A\ln x_A+(1-x_A)\ln(1-x_A)+x_B\ln x_B+(1-x_B)\ln(1-x_B)]\\&=\mu(\frac{x_A+x_B}{2})+3(2J_1+J_2)(\frac{x_A+x_B}{2})^2-\frac{3}{4}J_2(x_A-x_B)^2\\&+\frac{k_BT}{2}[x_A\ln x_A+(1-x_A)\ln(1-x_A)+x_B\ln x_B+(1-x_B)\ln(1-x_B)]\end{aligned} \tag{10.1}$$

where $x_A=x+\eta/2$ and $x_B=x-\eta/2$ are the site occupancies for sites on alternate $(111)_C$ cation planes. In equilibrium, the chemical potentials, μ_A and μ_B of the 2 sublattices must be equal because they can exchange particles. Therefore

$$\frac{\partial(F/N)}{\partial x_A}=\frac{\partial(F/N)}{\partial x_B}=0 \tag{10.2}$$

Thus

$$\frac{\mu}{2}+3J_1(x_A+x_B)+3J_2x_B+\frac{k_BT}{2}\ln\frac{x_A}{1-x_A}+E_0=0 \tag{10.3}$$

where E_0 is a constant and

$$\frac{\mu}{2} + 3J_1(x_A + x_B) + 3J_2 x_A + \frac{k_B T}{2} \ln \frac{x_B}{1 - x_B} + E_0 = 0 \qquad (10.4)$$

These equations are then arranged

$$\frac{x_A}{1 - x_A} = e^{-\varepsilon_A} \qquad \text{and} \qquad \frac{x_B}{1 - x_B} = e^{-\varepsilon_B} \qquad (10.5)$$

where

$$\varepsilon_A = \frac{2}{k_B T}\left[E_0 + \frac{\mu}{2} + 3J_1(x_A + x_B) + 3J_2 x_B\right] \qquad (10.6)$$

and

$$\varepsilon_B = \frac{2}{k_B T}\left[E_0 + \frac{\mu}{2} + 3J_1(x_A + x_B) + 3J_2 x_A\right] \qquad (10.7)$$

The equations (10.5-10.7) are easily solved by an iterative method and are used to find the relation of η versus x and the mean field phase diagram for the model.

Figure 11a shows η versus x in $Li_xNi_{2-x}O_2$ for $J_2/(k_BT)=0.78$ and for $J_2/(k_BT)=1.35$ (chosen so that the maximum in η agrees with the data) calculated by minimizing the Bragg-Williams free-energy given by equation (9.1). This can be directly compared to the data in Figure 9. The agreement is encouraging and suggests that better solutions to the statistical mechanics, such as Monte Carlo methods, are in order. Figure 11b shows the mean-field phase diagram for the model.

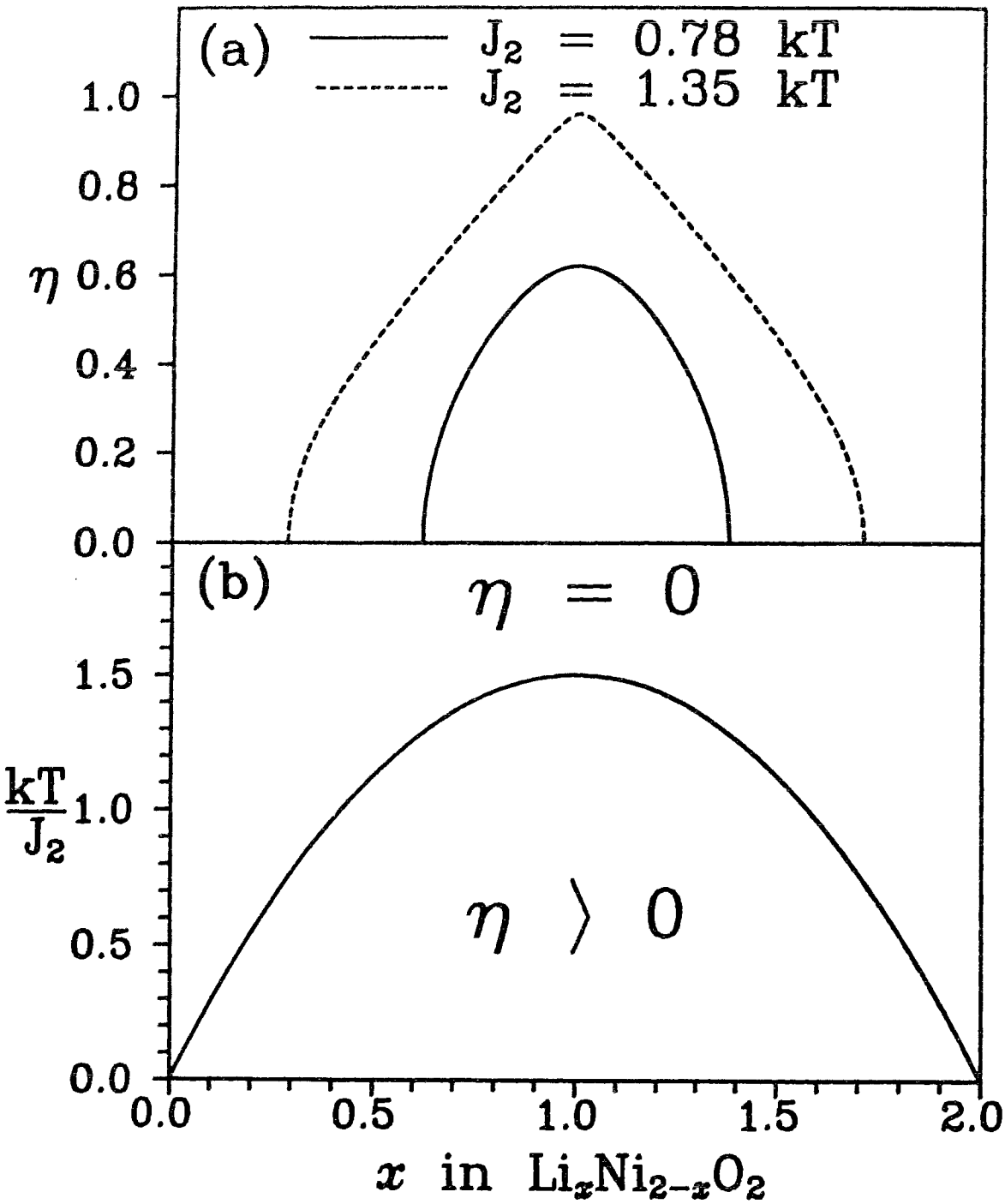

Fig. 11 (a) The order parameter versus x calculated by the Bragg-Williams model for the values of J_2/k_BT shown

(b) The order-disorder phase diagram calculated using the Bragg-Williams model

7 Monte Carlo Results

The Monte Carlo method [50] is now commonly used in physics. The name Monte Carlo comes from similarity of this method with roulette games that use random numbers. The Monte Carlo method does not use the same method as roulette games to produce the 10^{10} required random numbers but uses computers to create them in order to save time. The random numbers are then used for simulating configurations of the system.

In thermodynamic fluctuation theory, the distribution function of any macroscopic variable will be sharply peaked around its average value; e. g. , for the energy E itself, the distribution will be peaked at $\langle E \rangle_T$, which is proportional to N, while the width of the distribution will be proportional to $\sqrt{N}$. The Ising model is one of the typical samples studied with the Monte Carlo method. On a scale of energy per spin in Ising model, the width of the distribution shrinks to zero as $1/\sqrt{N}$ for N to infinity. Thus, at any temperature, a rather narrow region of the configuration space of the system contributes significantly to the averages; a very small fraction of the generated states would actually lie in this important region of configuration space.

In the Metropolis method, the sample is chosen with a probability proportional to the Boltzmann factor itself, i.e. , the states are distributed according to a Gaussian distribution around the appropriate average value. In the Ising model example, one starts with some initial spin configuration in

Ising model, Thermal fluctuations are simulated by repeating the following six steps again and again:

1) Choose one spin to be considered for flipping (S_i to $-S_i$)

2) Calculate the energy change ΔH relative to that flip.

3) If $\Delta H<0$, flip the spin, otherwise calculate the transition probability W defined by $W=\exp(-\Delta H/k_B T)$ for that flip

4) Generate a random number p between zero and unity

5) If $p<W$ flip the spin, otherwise do not flip

6) Calculate the averages as desired with the resulting configuration

In the lattice gas model, each site has two states, $x_i=0$ (empty) or $x_i=1$ (filled). The Hamiltonian is

$$H=\frac{1}{2}J_1\sum_{i,j}^{NN}x_i x_j+\frac{1}{2}J_2\sum_{i,j}^{NNN}x_i x_j+\sum_i \mu x_i \qquad (11.1)$$

If the site is empty, $x_i=0$, and the energy change on filling the site is

$$\Delta H=J_1\sum_{j}^{NN}x_j+J_2\sum_{j}^{NNN}x_j+\mu \qquad (11.2)$$

If the site is filled, $x_i=1$, and the energy change on emptying the site is

$$\Delta H=-J_1\sum_{j}^{NN}x_j-J_2\sum_{j}^{NNN}x_j-\mu \qquad (11.3)$$

For x_i=0, if $\Delta H<0$, fill the site. If $\Delta H>0$, generate a random number, P, between 0 and 1. If $exp\ [-\Delta H/k_BT]>P$, fill the site; otherwise, leave it alone. For x_i=1 if $\Delta H<0$, empty the site. If $\Delta H>0$, generate a random number P between 0 and 1. If $exp[-\Delta H/k_BT]>P$, empty the site; otherwise, leave it alone.

The FCC lattice is composed of four simple cubic lattices and has 4 atoms per unit cell. Our lattices ranged in size from a 4x4x4 unit cell to a 12x12x12 cell or from 256 atoms to 6912 atoms. The boundary condition in one dimension is

$$x_1=x_{L+1}$$

where L is the even number of FCC lattice in one dimension. It is important to save computer time in this calculation by labelling each neighbor or next neighbor site by one integer. However, it is much easier to locate a neighbor or a next neighbor site by four integers. Figure 12 shows the way to label the neighbor and next neighbor sites by four integers.

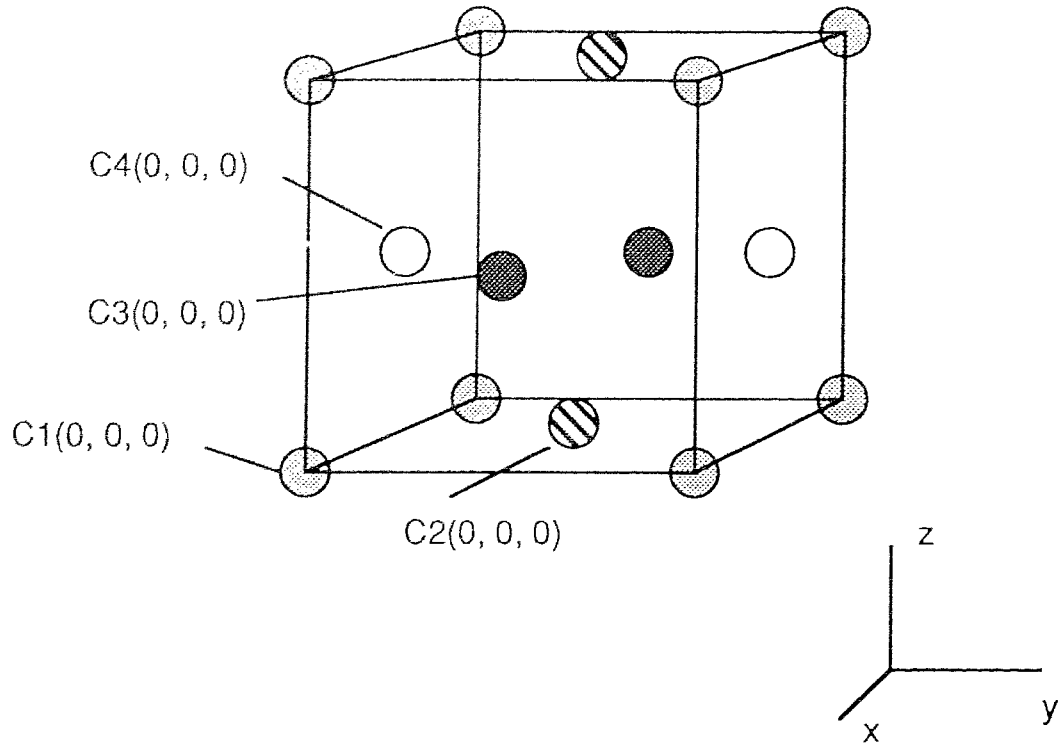

Figure 12 The FFC cubic structure is composed of four simple cubic lattices. Points on the same simple cubic lattices have the same color.

Any site can be labelled with the four integers (n, l_x, l_y, l_z), where $1<n<4$ is one of the 4 simple cubic lattices in the FCC structure and $1<l_x, l_y, l_z <L$ label the site position on the single cubic lattice. Hence the six next-nearest-neighbor sites of the site $C_n(0, 0, 0)$ are $C_n(1, 0, 0)$, $C_n(-1, 0, 0)$, $C_n(0, 1, 0)$, $C_n(0, -1, 0)$, $C_n(0, 0, 1)$ and $C_n(0, 0, -1)$. The twelve nearest-neighbors for $C_1(0, 0, 0)$ are $C_2(0, 0, 0)$, $C_2(1, 0, 0)$, $C_2(0, -1, 0)$, $C_2(1, -1, 0)$, $C_3(0, 0, 0)$, $C_3(0, -1, 0)$, $C_3(0, -1, -1)$, $C_3(0, 0, -1)$, $C_4(0, 0, 0)$, $C_4(0, 0, -1)$, $C_4(1, 0, 0)$, $C_4(1, 0, -1)$. The twelve nearest neighbors for $C_2(0, 0, 0)$ are $C_1(0, 0, 0)$, $C_1(0, 1, 0)$, $C_1(-1, 0, 0)$, $C_1(-1, 1, 0)$, $C_3(0, 0, 0)$, $C_3(-1, 0, 0)$, $C_3(-1, 0, -1)$, $C_3(0, 0, -1)$, $C_4(0, 0, 0)$, $C_4(0, 1, 0)$, $C_4(0, 0, -1)$, $C_4(0, 1, -1)$. The twelve nearest neighbors for $C_3(0, 0, 0)$ are $C_1(0, 0, 0)$, $C_1(0, 1, 0)$, $C_1(0,$

1, 1), C_1(0, 0, 1), C_2(0, 0, 0), C_2(0, 0, 1), C_2(1, 0, 0), C_2(1, 0, 1), C_4(0, 0, 0), C_4(0, 1, 0), C_4(1, 0, 0), C_4(1, 1, 0). The twelve nearest neighbors for C_4(0, 0, 0) are C_1(0, 0, 0), C_1(0, 0, 1), C_1(-1, 0, 0), C_1(-1, 0, 1), C_2(0, 0, 0), C_2(0, 0, 1), C_2(0, -1, 0), C_2(0, -1, 1), C_3(0, 0, 0), C_3(0, -1, 0), C_3(-1, 0, 0), C_3(-1, -1, 0).

We transfer the four numbers into one number for convenience in the calculation. Any l can be treated as $0 \le l \le L$ under the boundary condition.

Here we use the Monte Carlo method to calculate the order parameter versus x and T. As order develops, we do not know *a-priori* along which of the 4 equivalent cubic directions (1 1 1), (1 $\bar{1}$ 1), (1 1 $\bar{1}$) or (1 $\bar{1}$ $\bar{1}$) the order develops. To calculate the long range order parameter, we calculate the average site occupancy in layers normal to (111) and then take the difference between the average occupancies of the set of alternate planes. This we call η_1. We repeat this procedure for planes normal to the (1 $\bar{1}$ 1) (1 1 $\bar{1}$) and (1 $\bar{1}$ $\bar{1}$) directions, finding η_2, η_3 and η_4 respectively. In the ordered state, only one of the 4 order parameters is significantly different from zero. The overall order parameter, η is then defined to be

$$\eta = (\eta_1^2 + \eta_2^2 + \eta_3^2 + \eta_4^2)^{\frac{1}{2}} \qquad (12.1)$$

to ensure that our computation is sensitive to the development of long range order in any of the 4 possible directions and to ensure that η is positive.

Figure 13 shows η versus x in $Li_xNi_{2-x}O_2$ calculated for $J_2 = 1.2k_BT$ with $J_1 = -0.5k_BT$, for a variety of lattice sizes. At x=1, when the lattice is half filled by Li, the order parameter reaches a maximum of 0.92, which is approximately independent of lattice size. However, the order parameter depends on the lattice size near the critical composition, x_c. The finite sized lattice we use

shows residual order below x_c which decreases as the lattice size increases. Figure 14 shows $<\eta>$ versus x for $J_2 = 1.35 k_B T$ calculated by Monte Carlo (L=12) and mean field theory for $J_2 = 1.35 k_B T$ and $J_2 = 0.78 k_B T$. We see that mean-field theory can not fit the data both at $x=1$ and $x_c=0.62$ with the same J_2.

The data in figure 8 suggest that experimentally $x_c=0.62$ and the data in figure 9 show that the maximum in η at $x=1$ is $\eta_{max}=0.96$. Figure 14 also shows our attempt to fit the data with the Monte Carlo calculation using $J_2 = 1.35 k_B T$ (J_1 can be chosen within a wide range without affecting the results significantly) on the largest (12x12x12)lattice size considered. The fit is excellent in the ordered state which shows that $Li_xNi_{2-x}O_2$ can be well described by a lattice gas model.

The critical composition, x_c , where order develops, is most determined by plotting the fluctuations of the order parameter,

$$N(<\eta^2>-<\eta>^2) \qquad (12.2)$$

versus x . Noise free fluctuation quantities such as $<\eta^2> - <\eta>^2$ are very difficult to calculate with conventional Monte Carlo methods, particularly if successive spin configurations are highly correlated (auto-correlation). In order to alleviate this problem mentioned in reference [56], we have used Ferrenberg and Swendsen's *Multi-Histogram* method [51], which allows optimal use of all the simulation data.

The probability distribution at chemical potential μ, $P_\mu(x)$, is generated by building a histogram of the number of times the lattice gas configurations have x in the range x_i and $x_i+\Delta x$, where i labels a bin in the histogram and Δx

is the bin size. In this work we used $\Delta x=4\times10^{-5}$. From the re-weighting transformation

$$P_{\mu'}(x)=\frac{P_{\mu}(x)exp\{-\beta x(\mu'-\mu)\}}{\sum_{x}P_{\mu}(x)exp\{-\beta x(\mu'-\mu)\}} \qquad (12.3)$$

one can see that the exact probability distribution at μ actually contains all the necessary information needed to calculate $P_{\mu'}(x)$ for any other chemical potential μ′. In practice $P_{\mu}(x)$ only contains information on distributions for μ′ near μ, because of poor counting statistics in the wings of the histogram far from $\langle x\rangle_{\mu}$. However, data quality can be improved considerably by combining numerous histograms generated at different μ's.

In order to obtain an accurate estimate of x_c in reference [56], we have calculated the following three fluctuation quantities

$$N(\langle\eta^2\rangle-\langle\eta\rangle^2) \qquad (13.1)$$

$$N(\langle x^2\rangle-\langle x\rangle^2) \qquad (13.2)$$

$$N(\langle x\eta\rangle-\langle x\rangle\langle\eta\rangle) \qquad (13.3)$$

which all have maxima at the phase transition. Figure 15a shows the fluctuations in the order parameter η for three different lattice sizes, L=4, 8 and 12. Two other lattice sizes, L=6 and 10 (not shown) were also simulated. The solid lines in figure 15a are calculated using the multiple histogram method and discrete data points are obtained by standard averaging at each μ simulated. For each μ, 1000 mcs (Monte Carlo Step) were allowed for the system to reach equilibrium and a further 10000 mcs for averaging of

thermodynamic quantities. In order to estimate x_c in the thermodynamic limit we have extrapolated assuming a power law dependence on lattice size

$$x_c(L) = x_c(\infty) + AL^{-z} \tag{14}$$

The fits (figure 15b) were rather insensitive to the exponent z but the best results were obtained for $x_c(\infty)$=0.620(5) and z=1.5.

Figure 16 shows the phase diagram calculated by the Monte Carlo method with L=12. The phase transition point is taken at the point of maximum fluctuation of the order parameter. With J_1=-0.5k_BT, the ordered phase has the maximum k_BT/J_2=1.05 at x=1 and the minimum at x=0.4. Figure 17 shows the order parameters η versus x calculated by the Monte Carlo method with L=12 and J_1=-0.5k_BT. The order parameter η reaches 1 at x=1 for J_2/k_BT>1.6.

Figure 18 shows the effect of J_1 on the results of η versus x.. With J_2=1.35k_BT and L=12, changes in J_1, have a negligible effect on η for -0.5k_BT<J_1<0.5k_BT and do not effect x_c significantly. However, when J_1 becomes larger, especially when J_1>J_2, these changes are significant. At J_1=2.0k_BT, the ordered phase only occurs very near x=1.

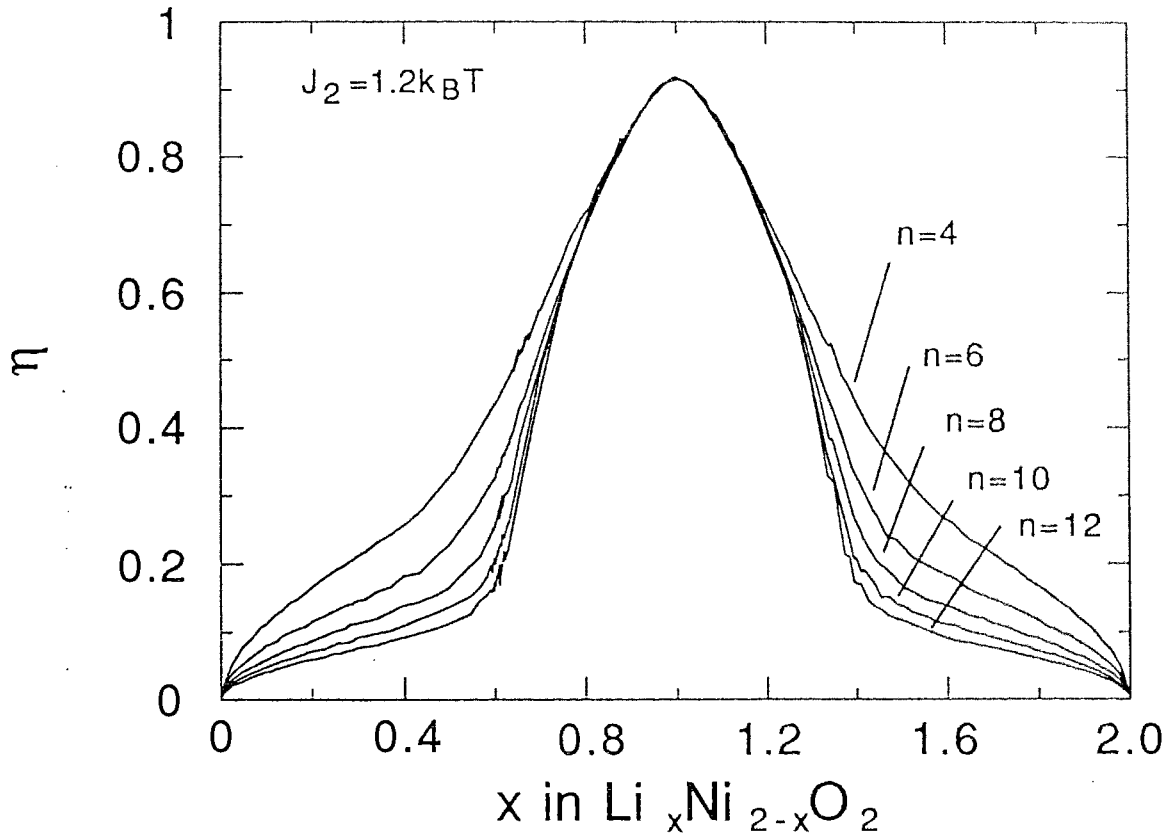

Fig. 13 The order parameter η from the Monte Carlo calculations for various lattice sizes and a fixed next-nearest-neighbor interaction constant. The results are averaged over of 1000 equilibrium ensembles

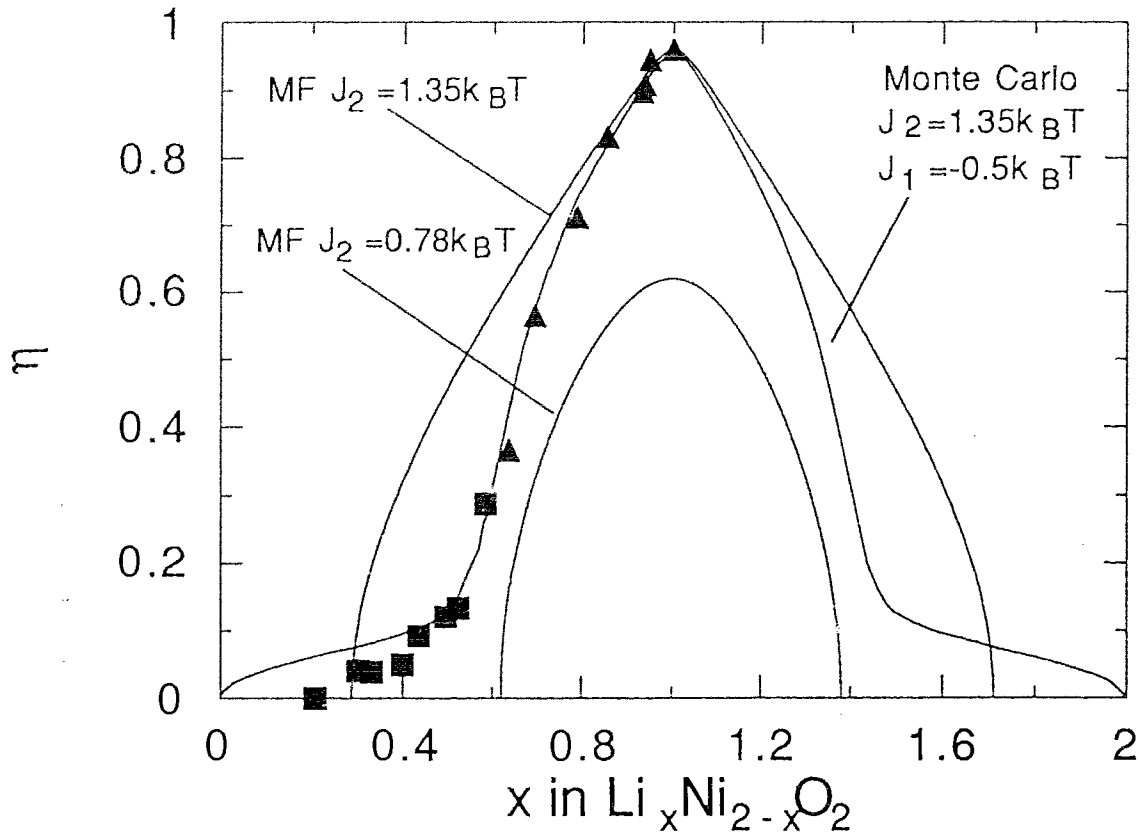

Fig. 14 Order parameter, η, versus x in $Li_xNi_{2-x}O_2$. The solid points are the data from figure 9 and the curves are from the Monte Carlo simulation (L=12) and the mean field theory

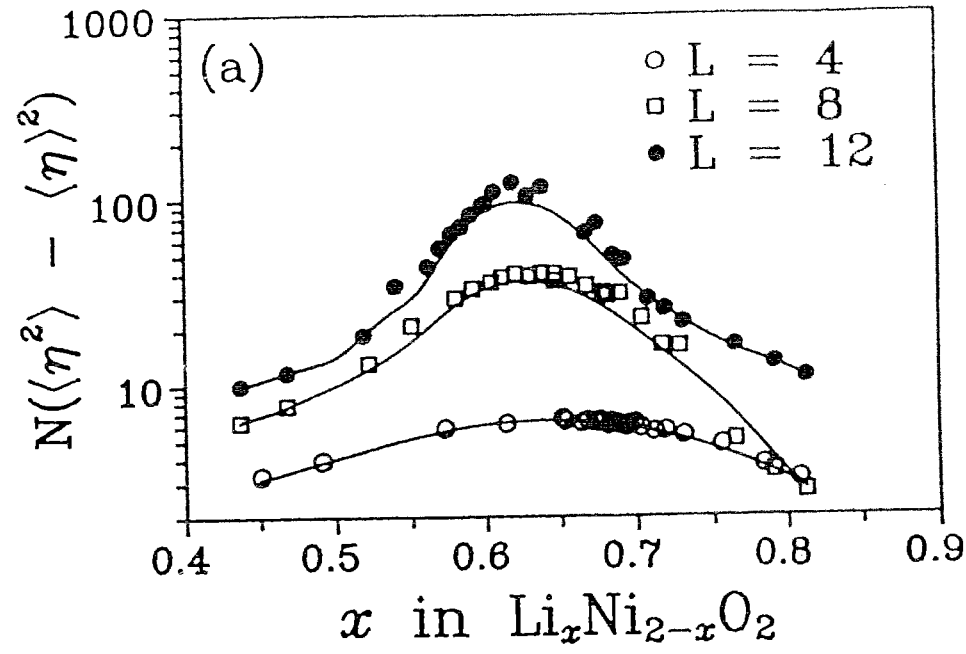

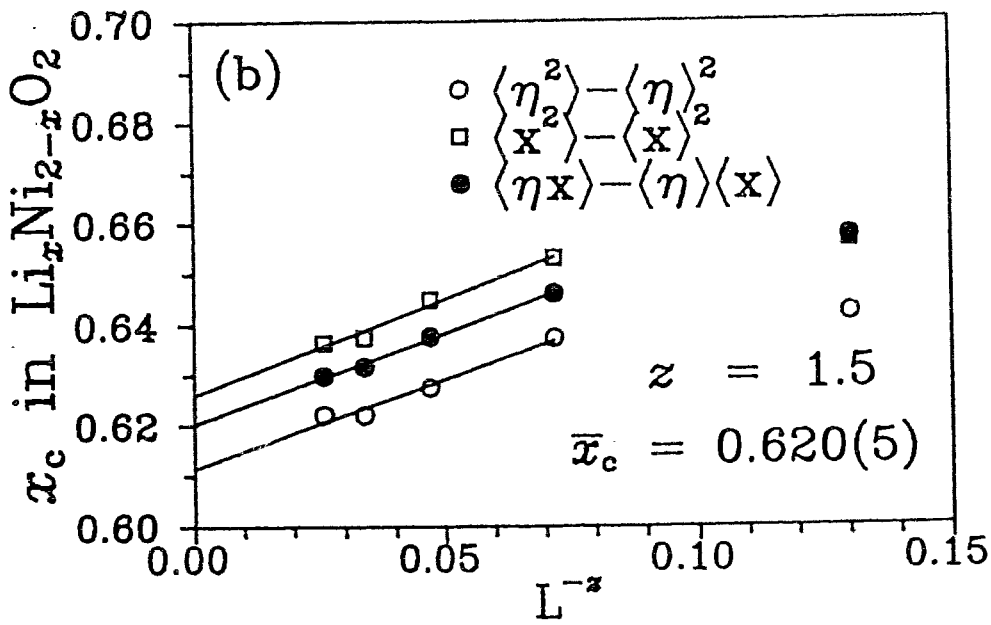

Fig. 15 (a) The fluctuations in the order parameter calculated from Monte Carlo averages (data points) and the Multi Histogram method (solid lines) for 3 lattice sizes. Averages and histograms generated from 10000 Monte Carlo steps at equilibrium for J_2=1.35kT and J_1=-0.5kT.

(b) Power law (see text) extrapolation of x_c to infinite lattice size giving x_c=0.620(5). x_c's for finite lattice sizes were calculated from 3 fluctuation quantities that all have maxima at the phase transition.

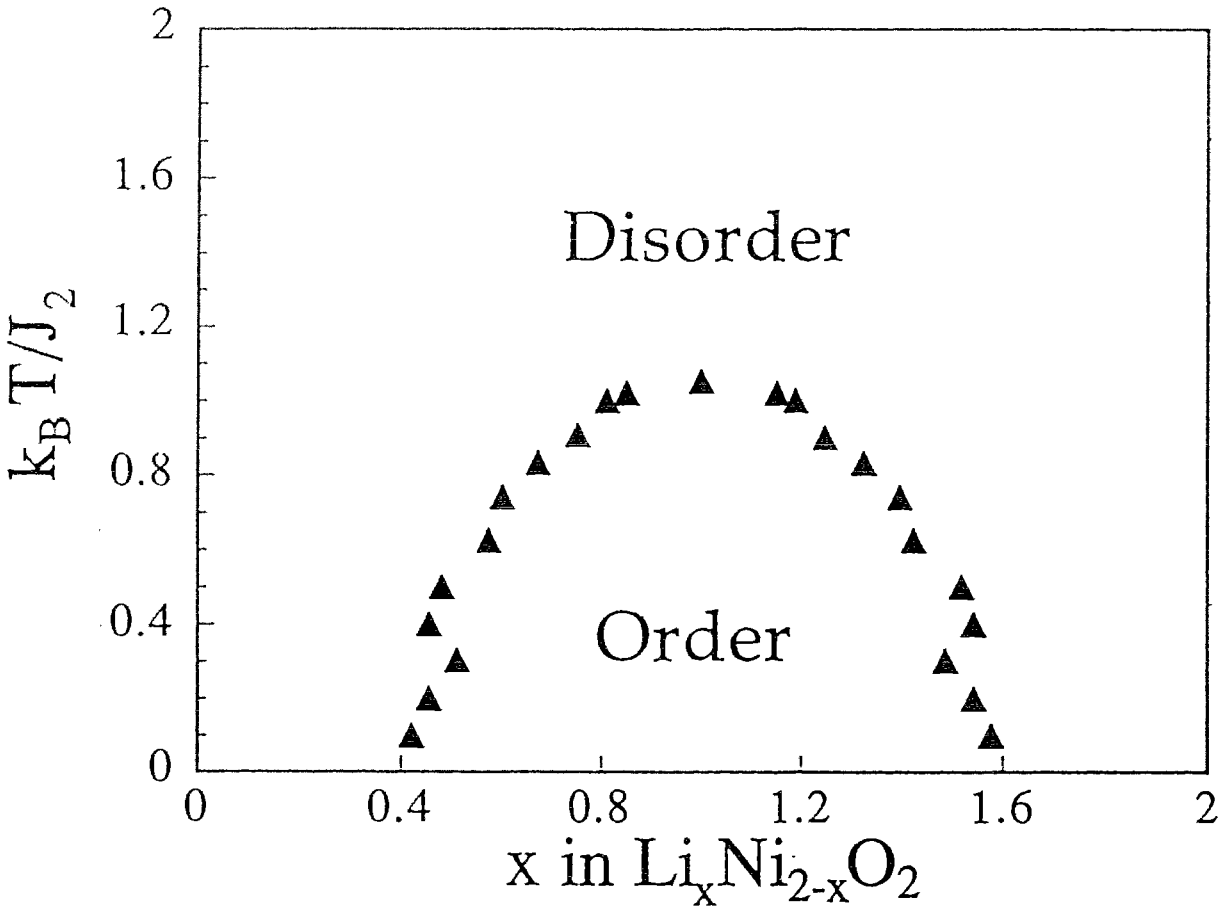

Fig. 16 The phase diagram is calculated by Monte Carlo method with L=12 and J_1=-0.5k_BT.

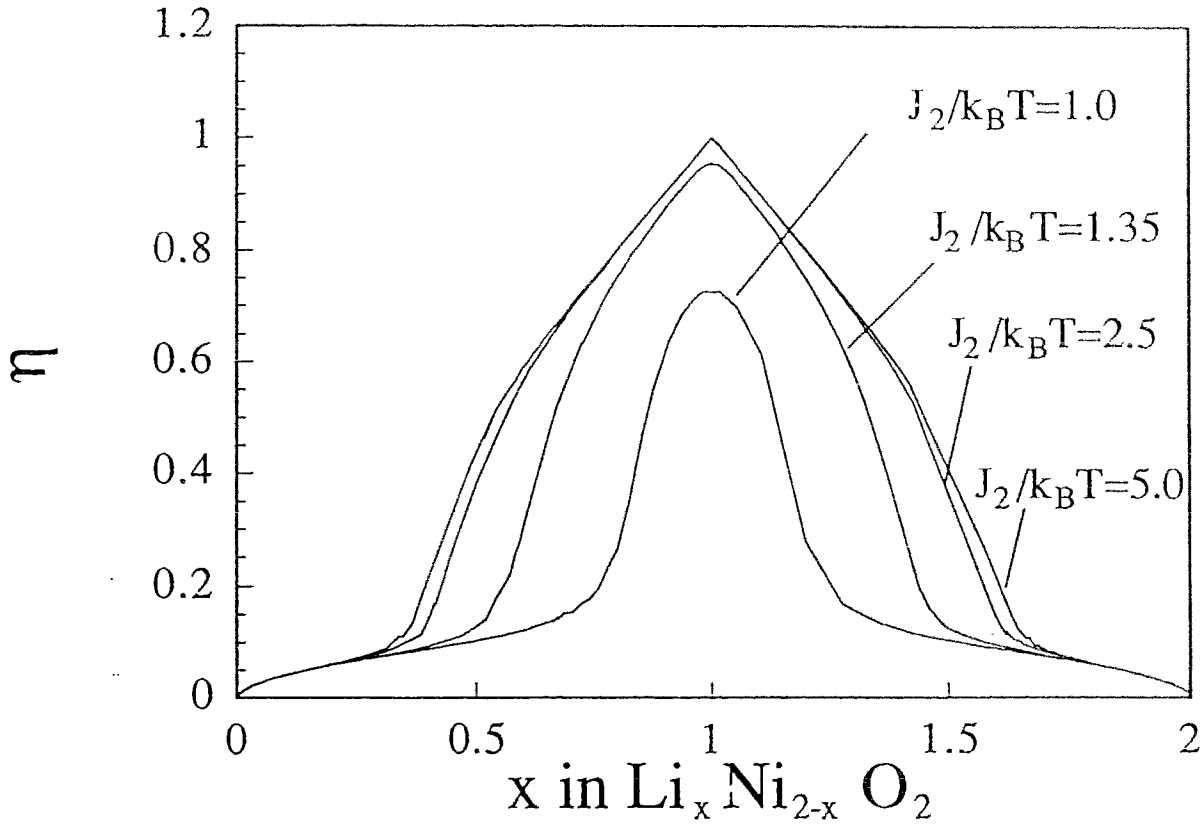

Fig. 17 The order parameters are calculated by Monte Carlo method for variety of J_2 with L=12 and J_1=-0.5k_BT.

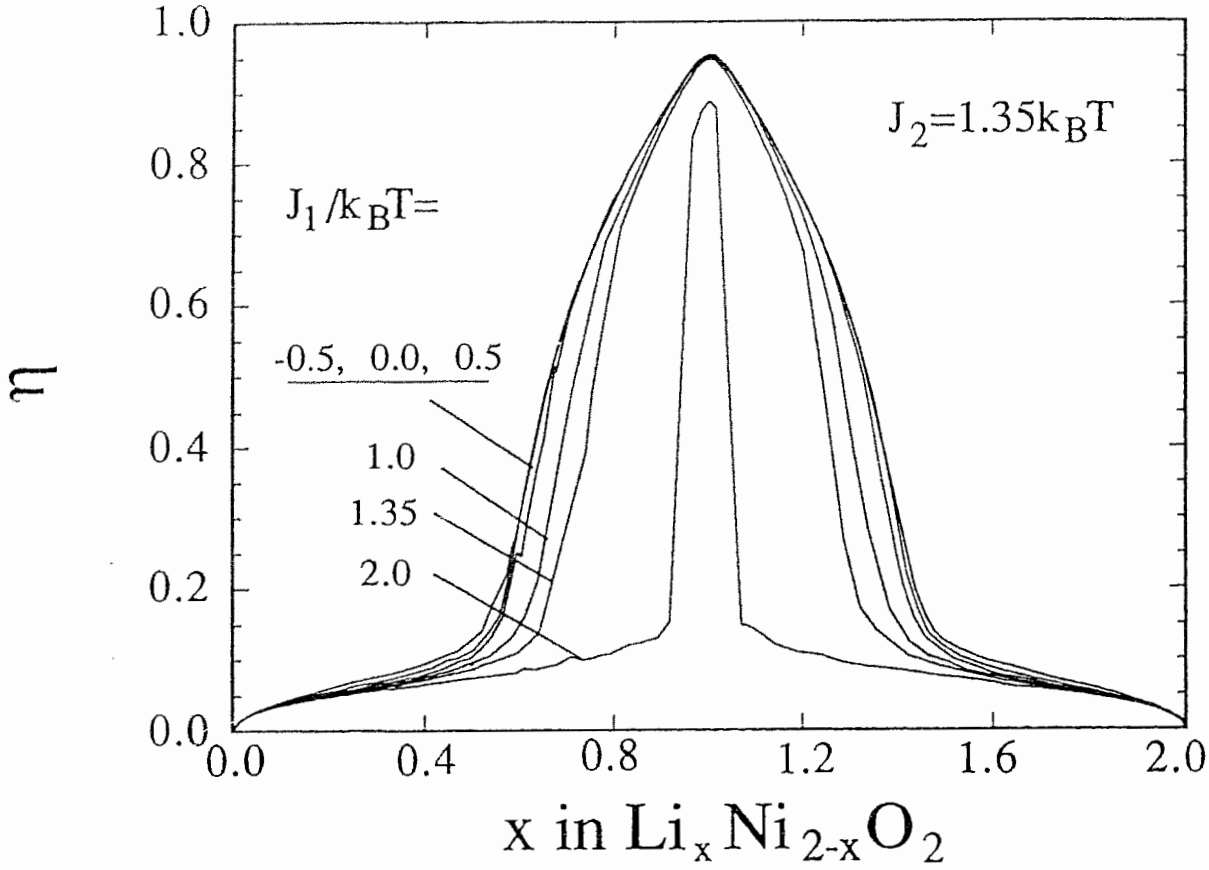

Fig. 18 The order parameters are calculated by Monte Carlo method for variety of J_1 with L=12 and J_2=1.35k_BT

8 Short-Range Order

Figure 19 shows the $(003)_H$ Bragg Peak region measured at several values of x in $Li_xNi_{2-x}O_2$. The data are displayed with different intensity scales, but this does not affect the peak shape. As x decreases below x=0.62, the width of the peak increases rapidly. The broad weak peak indicates the presence of short-range order, the precursor to the the long-range order which develops for x>0.62 as suggested in Figure 9. This short range order represents the tendency of Li atoms to avoid simultaneously filling next-nearest-neighbor sites.

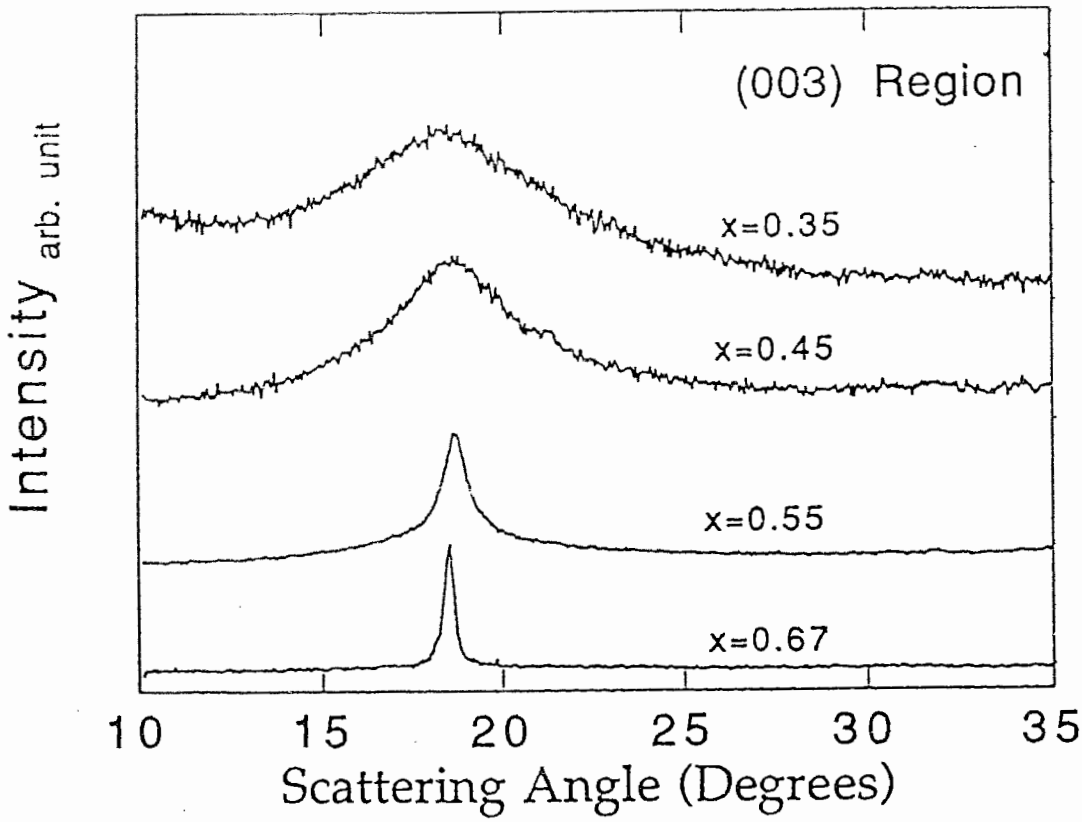

Fig. 19 X-ray diffraction shows the short-range order in $Li_xNi_{2-x}O_2$ for $0 \leq x \leq 0.62$. The Bragg peak in the $(003)_H$ region has been multiplied by a scale factor which increases as x decreases to make the peak visible at low x

9 Discussion

We have shown that the order-disorder transition in $Li_xNi_{2-x}O_2$ is well modelled by a lattice-gas treatment. Our model reproduces the data very well using $J_2 = 1.35 k_B T$ for small values of J_1 (e.g. $|J_1| < 0.5 k_B T$). These results clearly suggest that J_2 is larger that J_1 in this material. This is somewhat surprising since the cation-cation bond length corresponding to J_2 is $\sqrt{2}$ times that corresponding to J_1 and usually interaction strengths decrease with distance. However, the interactions J_1 and J_2 are made up of net Li-Li, Ni-Ni and Li-Ni interactions as given in equation (8.2), each of these interactions is very complicated to estimate.

We have know $J_2 = 1.35 k_B T$, and that the X-ray diffraction measurements reported here have been made at room temperature. It remains to determine the value of T (T≠Room Temperature). In our opinion, the important temperature is that at which the Ni atoms can no longer move. For the lattice gas treatment to be reasonable, both Li and Ni must be mobile and diffusing freely from site to site. During cooling of our samples the Ni atoms freeze at some temperature; (probably around 600˚C since synthesis of $LiNiO_2$ is very slow(>40hours) at this temperature); thus our samples are "snap shots" of the equilibrium that existed just above that temperature. Using T=600˚C, we calculate $J_2 = 0.11eV$. Preliminary high temperature diffraction measurements using an *in-situ* furnace show that the ordered phase in

$Li_{0.66}Ni_{1.34}O_2$ is reversibly suppressed at about 1000°C, consistent with our estimate of T above. Further high temperature work will be done later.

One goal of our research is to extract the cation-cation interaction energies so that we can model the behavior of Li/Li_xNiO_2 batteries with lattice-gas models as has been done previously for other intercalation compounds [53, 54]. Unfortunately, we have shown that the value of the nearest neighbor interaction, most important for that application, cannot be determined from the order-disorder in $Li_xNi_{2-x}O_2$ since the nearest neighbor interaction is not sensitive to the observed order parameter. Other measurements, such as the variation of the Li chemical potential in $Li_xNi_{2-x}O_2$ with x are needed to determine the Li-Li contribution to J_1.

The Li transition-metal oxides ($LiMO_2$) show a rich variety of structures based on close packed oxygen layers [52]. The Li and M atoms form a variety of ordered arrangements which can probably be explained by suitable choices of cation-cation interaction energies in a lattice-gas formalism. One of our future goals is to determine a set of interactions consistent with the observed structures.

Appendix

The following is an argument that entropy is maximized when only one of the four degenerate order parameters η_1, η_2, η_3, or η_4 is selected, we must write the general site occupancy as

$$x_i = x + \frac{1}{2}\sum_{\alpha=1}^{8} \eta_{q_\alpha} \exp(i\mathbf{q}_\alpha \cdot \mathbf{r}_i) \tag{A1}$$

where x is the uniform site occupation. $\mathbf{r}_i$ is the lattice vector for site i, and the $\mathbf{q}_\alpha$ are the eight ordering wavevectors, $\mathbf{q}_1=(1, 1, 1)$, $\mathbf{q}_2=(1, \bar{1}, \bar{1})$, $\mathbf{q}_3=(\bar{1}, 1, \bar{1})$, $\mathbf{q}_4=(\bar{1}, \bar{1}, 1)$, $\mathbf{q}_5=-\mathbf{q}_1$, $\mathbf{q}_6=-\mathbf{q}_2$, $\mathbf{q}_7=-\mathbf{q}_3$, $\mathbf{q}_8=-\mathbf{q}_4$. Reality of the x_i implies the following constraint

$$\eta_{q_\alpha} = \eta^*_{-q_\alpha} \tag{A2}$$

Thus $\eta_{q_1} = \eta^*_{q_5}$ and we define $\eta_1 = \eta_{q_1} + \eta^*_{q_5}$ with similar relationships for the other 3 order parameters. Substituting (A1) into the Landau expansion (9.2) we obtain

$$F/N = \mu x + 3(2J_1 + J_2)x^2 + (\frac{k_B T}{8}\frac{1}{x(1-x)} - \frac{3}{4}J_2)(\eta_1^2 + \eta_2^2 + \eta_3^2 + \eta_4^2)$$
$$+ \frac{k_B T}{192}(\frac{1}{x^3} + \frac{1}{(1-x)^3}) f^{(4)} \tag{A3}$$

where

$$f^{(4)} = \sum_{\alpha\beta\gamma\varepsilon} \eta_\alpha \eta_\beta \eta_\gamma \eta_\varepsilon \delta(\mathbf{q}_\alpha + \mathbf{q}_\beta + \mathbf{q}_\gamma + \mathbf{q}_\varepsilon) \tag{A4}$$

where $\delta(q_\alpha + q_\beta + q_\gamma + q_\varepsilon)$ is a discrete delta function. Expanding the fourth order term (A4), we have

$$f^{(4)} = 24(\sum_\alpha \eta_\alpha^4 + 3\sum_{\alpha\neq\beta} \eta_\alpha^2 \eta_\beta^2 + 2\eta_1\eta_2\eta_3\eta_4)$$
$$= 24(3|\sum_\alpha \eta_\alpha^2|^2 - 2\sum_\alpha \eta_\alpha^4 + 2\eta_1\eta_2\eta_3\eta_4), \qquad \text{(A5)}$$

which determines whether one η_α is selected or not. In order to make a meaningful comparison of free energies, the values of the η_α must be chosen so as to satisfy

$$\eta_1^2 + \eta_2^2 + \eta_3^2 + \eta_4^2 = \eta^2 \qquad \text{(A6)}$$

For simplicity, we will test the two extreme cases for which (A6) is satisfied:

Case 1: $\eta_1=\eta_2=\eta_3=\eta_4=\eta/2$

$$f^{(4)} = 24(3\eta^4 - \frac{1}{2}\eta^4 + \frac{1}{8}\eta^4) = 63\eta^4 \qquad \text{(A7)}$$

Case 2: $\eta_1=\eta$, $\eta_2=\eta_3=\eta_4=0$

$$f^{(4)} = 24(3\eta^4 - 2\eta^4) = 24\eta^4 \qquad \text{(A8)}$$

Since the coefficient of the fourth order term is positive definite and (A8)<(A7), the free energy is lower for case 2 than for case 1, *i.e.* only *one* of the four η's will be selected.

Refereces

[1]. Johann Desilvestro and Otto Haas, J. Electrochem. Soc. **137**, 5c (1990)

[2]. J. R. Dahn, submitted to Chapter for Handbook of Batteries and Fuel Cells

[3]. R. Fong, U. Von Sacken and J. R. Dahn, J. Electrochem Soc. **137**, 2009 (1990)

[4]. J. R. Dahn, U. Von Sacken, M. W. Juzkow and H. Al-Janaby, J. Electrochem. Soc. **138**, 2207 (1991)

[5]. T. Nagaura and K. Tozawa, Progress in Batteries and Solar Cell **9**, 209 (1990)

[6]. J. T. Dudley et al., J. Power Sources **35**, 59 (1991)

[7]. Avd. Batt. Technol. **25**, No. 10, 59 (1991)

[8]. K. M. Abraham, J. Power Source **7**, 1 (1981)

[9]. G. Voorn, J. Power Sources **14**, 135 (1985)

[10]. Y. Sakurai, S. Okada, J. Yamaki and T. Okada, *ibid.*, **20**, 172 (1987)

[11]. K. Nassau and D. W. Murphy, J. Non-Cryst. Solids **44**, 297 (1981)

[12]. S. Panero, M. Pasquali and G. Pistoia, J. Electrochem. Soc. **130**, 1225 (1983)

[13]. G. Pistoia, M. Pasquali, M. Tocci, V. manev and R. V. Moshtev, J. Power Source **15**, 13 (1985)

[14]. D. W. Murphy, P. A. Christian, F. J. DiSalvo and J. N. Carides, J. Electrochem. Soc. **126**, 497 (1979)

[15]. K. West, B. Zachau-Christiansen and T. Jacobsen, Electrochim. Acta, **28**, 1829 (1983)

[16]. K. M. Abraham, J. L. Goldman, and M. D. Dempsey, J. Electrochem. Soc. **128**, 2493 (1981)

[17]. B. Besenhard, J. Heydecke, E. Wudy, and H. P. Fritz, Solid State Ionics **8**, 61 (1983)

[18]. D. Linden in "Handbook of Batteries and Fuel Cells" D. Linden Editor, p. 11-1, McGraw-Hill, Inc. New York (1984)

[19]. Y. Toyoguchi, J. Yamaura, T. Matsui and J. Iijima, Abstract 73, p. 109, The Electrochemical Society Extended Abstracts Vol. 87-2, Honolulu, HI Oct. 18-23 (1987)

[20]. O. Yamamoto, Y. Takeda, R. Kamno, Y. Oyabe and Y. Shiuya, *ibid.*, **20**, 151 (1987)

[21]. K. Kordesch, W. Harer, W. Taucher and K. Tomantscher in "Proceedings of 22nd Intersociaty Energy Conversion Engineering Confereence" Vol. 2, p. 1102 (1987)

[22]. H. Ikeda in " Lithium Batteries", J-P Gabano, Editor, p. 169, Academic Press, Lit., London (1983)

[23]. Battery & EV Technol. **12** (7), 2 (1988)

[24]. S. U. Falk and A. J. Salkind "Alkaline Storage Batteries" Wiley, New York (1969)

[25]. K. Mizushima, P. C. Jones, P. J. Wiseman and J. B. Goodenough, Mater. Res. Bull. **15**, 783 (1980)

[26]. M. G. S. R. Thomas, P. G. Bruce and J. B. Goodenough, Solid State Ionics **18/19**, 794 (1986)

[27]. "Cellular Phone Recall May Cause Setback for Moli", Toronto Globe and Mail August 15, 1989 (Toronto Canada)

[28]. J. R. Dahn, Ulrich von Sacken and C. A. Michal, Solid State Ionics **44**, 87 (1990)

[29]. K. West, B. Zachau-Christiansen, M. J. L. Ostergard and T. Jacobsen, J. Power Sources **20**, 165 (1987)

[30]. L. D. Dyer, B. S. Borie and G. P. Smith, J. Am. Chem. Soc. **78**, 1499 (1958)

[31]. J. B. Goodenough, D. G. Wickham and W. J. Groft, J. Appl. Phys. **29**, 382 (1958)

[32]. J. B. Goodenough, D. G. Wickham and W. J. Croft, J. Appl. Phys. **29**, 382 (1958)

[33]. V. W. Bronger, H. Bade and W. Klemn, Z. Anorg. Allg. Chem. 333, 188 (1964)

[34]. H. Rieck and R. Hoppe, Z. Anorg. Allg. Chem. **392**, 193 (1972)

[35]. M. G. S. R. Thomas, W. I. F. David, and J. B. Goodenough, Mat. Res. Bull. 20, 1137 (1985)

[36]. K. Otsuka and T. Komatsu, J. Chem. Soc., Chem. Commun. 388, (1987)

[37]. G. L Semin, A. E. Cherkashin and N. P. Keier, React. Kinet. Catal. Lett. 1, 253 (1974)

[38]. T. Ito, J-X. Wang, C-H Lin and J. H. Lunsford, J. Amer. Chem. Soc. 107, 5062 (1985)

[39]. F. C. Nix and W. Shockley, Rev. Mod. Phys. 10, 1 (1938)

[40]. H. Lipson, Prog. Metal Phys. 2, 1 (1950)

[41]. L. Guttman, Solid State Phsy. 3, 145 (1956)

[42]. V. Gerold, Erg. d. Exakten Naturu. 33, 105 (1961)

[43]. B. E. Warren, X-ray Diffraction, Addison-Wesley Publishing Company, (1969)

[44]. R. J. Hill, C. J. Howard, Program for Rietveld Analysis of Fixed Wave Length X-ray and Neutron Powder Diffraction Patterns-Version LHPM1, AAEC (Lucas Heights Research Laboratories N. S. W., Australia)

[45]. H. M. Rietveld, Acta Crystallogr. 22, 151 (1967)

[46]. D. B. Wiles, R. A. Young, J. Appl. Crystallogr. 14, 149 (1981)

[47]. G. Caglioti, A. Paoletti, F. P. Ricci, Nucl. Instrum., 3, 223 (1958)

[48]. J. M. Ziman, Models of Disorder (Cambridge University Press, New York 1979)

[49]. J. S. Smart, Effective Field Theories of Magnetism (Saunders Philadelphia, P. A. 1966)

[50]. K. Binder, Monte Carlo Methods in Statistical Physics in Statistical Physics (Springer-Verlag, 1986)

[51]. A. M. Ferrenberg and R. H. Swendsen, Phys. Rev. Lett. **61**, 2635 (1988), A. M. Ferrenberg and R. H. Swendsen, Phys. Rev. Lett. **63**, 1195 (1989), A. M. Ferrenberg and R. H. Swendsen, Computers in Physics Sep./Oct. 101 (1989)

[52]. T. A. Hewston and B. L. Chambe land, J. Phys. Chem. Solids **48**, 97(1987)

[53]. J. R. Dahn and W. R. Mckinnon, J. Phys. C. **17**, 1423 (1984)

[54]. S. T. Coleman, W. R. Mckinnon and J. R. Dahn, Phys. Rev. B. **29**, 4147 (1984)

[55]. J. N. Reimers, J. R. Dahn, J. E. Greedan, C. V. Stager, G. Lin, I. Davidson, U. von Sacken. submitted to Phys. Rev. B

[56]. W. Li, J. N. Reimers, J. R. Dahn, submitted to Phys. Rev. B